ASSESSMENT OF THE ICING CHARACTERISTICS OF SINGLE AND COAXIAL ROTORS

A Dissertation
Presented to
The Academic Faculty

by

Nana Obayashi

In Partial Fulfillment
of the Requirements for the Degree
Master of Science in the
Daniel Guggenheim School of Aerospace Engineering

Georgia Institute of Technology
December 2016

ASSESSMENT OF THE ICING CHARACTERISTICS OF SINGLE AND COAXIAL ROTORS

Approved by:

Dr. Lakshmi N. Sankar, Advisor
School of Aerospace Engineering
Georgia Institute of Technology

Dr. Jechiel I. Jagoda
School of Aerospace Engineering
Georgia Institute of Technology

Dr. Daniel P. Schrage
School of Aerospace Engineering
Georgia Institute of Technology

Date Approved: November 14, 2016

ACKNOWLEDGEMENTS

I would like to express my sincere gratitude to my advisor, Prof. Lakshmi Sankar for his support and guidance throughout my years at Georgia Tech. It has been my pleasure to pursue my studies with him and he has been a great inspiration. My appreciation also goes to the members of my thesis committee, Prof. Jeff Jagoda and Prof. Daniel Schrage.

I would like to thank my colleagues, both past and present, especially of the Computational Fluid Dynamics Lab for their support and friendship. A special thanks go to Dr. Jeewoong Kim (ART Inc.) for his kind advising throughout the entire phase of this research, to Ms. Chong Zhou for providing extensive assistance with coursework and Star-CCM+, and to Mr. Phillip Huwiler for his continuous support and insightful comments.

Last but not least, I would like to thank my friends and family for their unconditional love and support. To my parents, Masatake and Satoko, I give my heartfelt appreciation for always encouraging me in all of my pursuits and being the source of strength.

This investigation was supported by the U.S. Army, NASA, and the Vertical Lift Research Centers of Excellence at Georgia Institute of Technology and Pennsylvania State University.

TABLE OF CONTENTS

LIST OF TABLES

LIST OF FIGURES

LIST OF SYMBOLS AND ABBREVIATIONS

B	Height of ice on substrate
C_p	Specific heat
D	Rotor diameter
d	Droplet diameter
FM	Figure of merit
Fr	Froude number, $U_\infty/\sqrt{Lg}$
h	Height of water on substrate
h/D	Rotor separation
k	Thermal conductivity
K	Inertia factor, $\rho d^2 U_\infty/18L\mu$
L_F	Latent heat of solidification of water
LWC	Liquid water content
MVD	Median volumetric diameter
r/R	Blade radial location
R	Rotor radius
R_k	Roughness Reynolds number
RPM	Revolutions per minute
T	Temperature of ice on substrate
T_s	Static air temperature
u	Dimensionless velocity
V_∞	Freestream air velocity
V_{tip}	Rotor tip velocity

α	Volume fraction
β	Collection efficiency
δ_3	Pitch-flap coupling angle
μ	Dynamic air viscosity
θ	Temperature of water on substrate
ρ	Density
σ	Solidity
2-D	Two dimensional
3-D	Three dimensional
ABC	Advancing blade concept
CFD	Computational fluid dynamics
DES	Detached Eddy simulation
k-ω	k-omega turbulence model
SA	Spalart-Allmaras turbulence model

SUMMARY

Icing on blade surfaces adversely affects the aerodynamic performance and safety of helicopters through loss of lift, loss of power, increase in drag, decrease in stall angle and dangerous ice shedding events. Equipping rotor blades against the effects of icing increases the helicopter cost and puts higher demand on the power plant. In the field of CFD, efforts have focused on modeling the effects of icing, including the resulting rotor performance degradation. Single rotor helicopters have been the primary focus of existing models for ice accretion, leaving an opportunity to expand modeling efforts to other types of helicopters, such as coaxial rotors. Although the coaxial rotor has a number of advantages attributed to its symmetric aerodynamic environment in any flight direction, additional work is needed using physics-based models, in order to analyze the complex flow interactions between the upper and lower blades.

An in-house ice accretion model was improved upon prior work by implementing a 3-D Eulerian approach integrated into the CFD flow solver, GT-Hybrid, in order to solve for water droplet collection efficiency on the surface of the rotor blade. This model implements an extended Messinger model with the Stefan condition at the ice/water interface in order to predict ice accretion based on droplet collection and establishment of a thermodynamic balance for phase shift. These improvements have allowed this model to reduce the limitations and empiricism inherent in existing models. The model has been validated based on a limited number of cases with promising predictive power compared to the industry standard ice accretion model by NASA, called LEWICE.

The present work contributes to the efforts behind the in-house ice accretion model in two ways. First, ice shape prediction using the in-house model was validated against existing experimental ice accretion data for a single rotor configuration in three different flight conditions. An analysis of the simulated and experimental results presented showed promising evidence of the model's predictive power, especially at the inboard blade locations where the ice is predominantly rime. Second, the in-house model was adapted for application to a coaxial rotor configuration. In order to validate the flow solution, performance analysis was completed for a coaxial rotor in hover using GT-Hybrid and Star-CCM+ in the absence of ice accretion and compared to existing experimental data on coaxial rotor performance. Then, ice accretion was simulated for the same rotor for three collective pitch angles and the ice shapes were presented. Finally, the performance degradation of the coaxial rotor due to ice was estimated.

CHAPTER 1. INTRODUCTION

In this section, some of the background information about ice formation on helicopters is listed, as well as the motivation behind this study. Background on coaxial rotors is also given, as ice studies using a coaxial configuration has not been addressed thus far to the author's knowledge. This section also contains useful resources about previous studies conducted on rotorcraft icing and coaxial rotor performance. Finally, the objectives for this study is presented.

1.1 Background and Motivation

Icing adversely affects the aerodynamic performance and safety of helicopters through loss of lift, loss of power, increase in drag, decrease in stall angle and dangerous ice shedding events. Equipping rotor blades against the effects of icing increases the helicopter cost and puts higher demand on the power plant. Considerable work has been done to develop analytical and empirical tools, along with experimental wind tunnel and flight test data, to understand the effects of icing. In the field of CFD, efforts have focused on modeling and simulating the effects of icing including the resulting rotor performance degradation. Significant progress has been made to model airflow over airfoils with prescribed ice shapes, collection efficiency of water droplets on the blade surface, ice accretion, ice shedding and its trajectory, and de-icing. Still more work remains to be done to validate existing models as well as to improve their predictive power.

Modern helicopters, both civilian and military operate in various weather conditions. Ice accretion may occur on the helicopter blade surfaces which are at below

freezing temperature, when supercooled water droplets from the clouds impinge on them. When ice accumulates on the blade leading edge, there are serious hazards, as the original aerodynamic configuration is drastically altered, as well as the corresponding flow field, and autorotational qualities. This results in a reduction of sectional lift coefficient and sectional pitching moment [1, 2, 3]. Furthermore, since ice formation is usually not uniform but creates a rough or spiked surface, the blade profile drag is increased and flow separation occurs prematurely. Then, the required torque to maintain flight increases, forcing the vehicle to operate near or even beyond the limits of its transmission [4, 5].

1.1.1 Background on Coaxial Rotors

Single rotor helicopters have been the primary focus of existing models for ice accretion, giving an opportunity to expand modeling efforts to other types of helicopters, such as coaxial rotor or tandem rotor aircrafts. Although coaxial rotor has a number of advantages attributed to its symmetric aerodynamic environment in any flight direction, additional work is needed using physics-based models, in order to analyze the complex interactions between the upper and lower blades.

A contrarotating coaxial rotor configuration is beneficial because the net size of the rotor is reduced for a given gross weight of the helicopter, compared to other configurations. The two rotors can achieve the necessary torque balance without a tail rotor, which serves an anti-torque purpose for single rotor helicopters. Both of the rotors can be used to produce useful vertical thrust. However, the wakes of the upper and lower rotor interact with each other, which may lead to a loss of net rotor system aero efficiency [6]. Due to this complex flow field compared to single rotor, high-fidelity methods must be

used to analyze the upper and lower rotor flow interactions and its effects on ice formation and the resulting performance degradation.

1.2 Previous Research

1.2.1 Studies on Rotorcraft Ice Accretion

Rotorcraft icing research was initially conducted experimentally in wind tunnels or during flight tests. In 1981 and 1983, icing experiments were conducted at the SIMA wind tunnel in France [7] using the Eurocopter Super Pima model rotor by varying numerous operation parameters. It was observed that speed and temperature have the most prominent effects on ice shape. Throughout 1983 and 1984, flight tests were conducted for the UH-1H in icing conditions by a joint NASA and Army Helicopter Icing Flight Test (HIFT) program [8]. Very different ice shapes were observed between level flight and hover flight. In 1988, rotor icing tests were conducted at the NASA Lewis Research Center Icing Research Tunnel (IRT) [4] for the first time. The OH-58 tail rotor rig was used and the experiments validated the IRT's ability to produce meaningful data for rotor testing.

NASA has developed an ice accretion tool called LEWICE [9] and it has become the most broadly accepted tool of its kind, while many researchers have developed methodologies to investigate the rotorcraft icing phenomena. Flemming [10] developed empirical relationships between ice thickness and aerodynamic force and moment coefficients for rotorcraft blades. Britton [11] developed an analytical method using the Interactive Boundary Layer approach [12] to calculate the performance degradation for an iced rotor blade, where the ice shapes were obtained by LEWICE. Zanazzi [13] performed ice growth simulations for 2-D radial sections of the blade using the classical Lagrangian

and the Messinger approach. He then used CFD tools to predict the performance degradation for the iced rotor configurations in hover. The methodology that this study uses is built upon Zanazzi's approach, as well as studies by Bain [14] and Narducci [15, 16].

1.2.2 Studies on Coaxial Rotors

Coleman [17] gives a good summary on aerodynamic issues peculiar to coaxial rotors that were tested in the United States, Russia, Germany, United Kingdom, and Japan. Within the United States, Taylor [18] tested a 1.67 ft diameter coaxial rotor in a static-thrust condition in 1950 and visualized flow using balsa dust and photographing the results. He found that the upper and lower rotor wakes contract at a faster and slower rate respectively, than when tested with an isolated rotor. Harrington [19] tested two coaxial rotor configurations, each with a 25 ft diameter. One of his configurations, Rotor 2 is modeled in this study. In the experiments, the hover theory for single rotors only gave a slight error for the coaxial configurations at the tested thrust settings. Dingledein [20] tested Harrington's Rotor 1 configuration in forward flight for constant thrust setting and rotor speed for several advance ratios. For the coaxial rotor, he saw an increase in profile and induced losses due to the upper and lower rotor interactions, causing an increase of up to 14% in required power compared to a single rotor configuration. Several numerical analyses in aerodynamics have been done for coaxial rotors [21, 22, 23], but to the author's knowledge, ice accretion simulations have yet to be completed.

1.3 Objectives

The work presented is based upon an ice accretion model put forth by Kim and Sankar [24]. This model was improved upon prior work by implementing a 3-D Eulerian approach integrated into the CFD flow solver in order to solve for water droplet collection efficiency on the surface of the rotor blade. This model implements also an extended Messinger model based on the Stefan condition in order to predict ice accretion based on droplet collection and establishment of a thermodynamic balance. These improvements have allowed this model to reduce the limitations and empiricism inherent in existing models. The model has been validated based on a limited number of cases run and showed promising predictive power compared to the industry standard ice accretion model by NASA, called LEWICE.

This work sets to make a number of contributions to the ice accretion modeling. The following will be contributions made for single rotor blade modeling:

- Model set forth by Kim and Sankar [24] is validated for three forward flight cases for which experimental data is available.

For coaxial rotors, this work sets forth to make the following contributions to the research on ice accretion modeling:

- Flow field solver called GT-Hybrid is used to model the flow for a coaxial rotor for a range of collective pitch angles for the upper rotor and validated using a wake-capturing analysis by Star-CCM+.
- Ice shapes will be predicted for select cases using the in-house ice accretion module.
- Ice shapes will also be used to estimate the performance degradation as a result of uneven ice accumulation for the blades.

CHAPTER 2. NUMERICAL FORMULATION

The solvers used for the ice shape simulation is discussed in this section. The procedure starts with a grid generation, followed by flow analysis using a CFD solver for a clean rotor configuration. The droplet solver then reads the flow field data in order to calculate the local collection efficiency, β, a measure of how much water collects on the blade surface. The ice formation can be simulated over time using the ice accretion solver. The overall procedure of developing the ice accretion model is shown in Figure 1 [24]. These solvers are coupled using a Python script, and the flow field and grid data are in PLOT3D format.

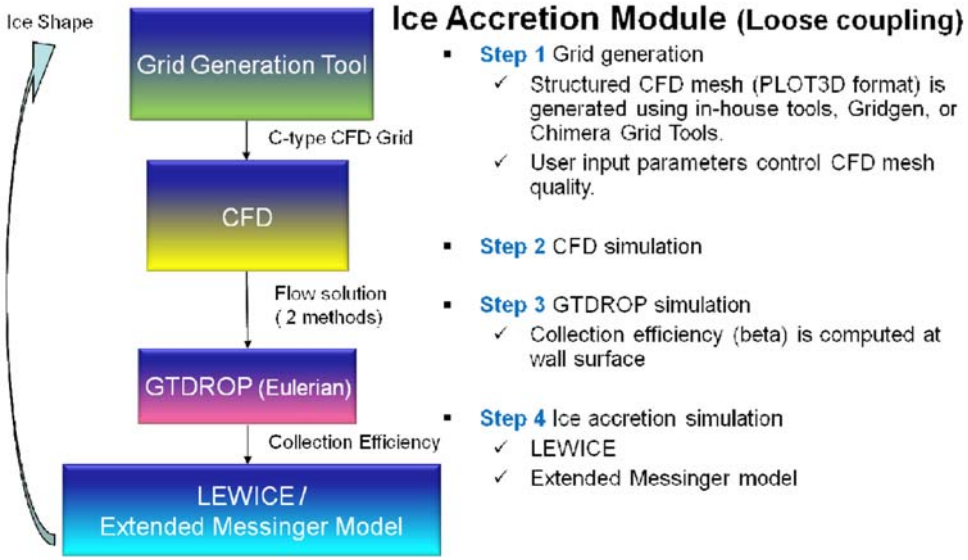

Figure 1 – Workflow of the ice accretion module.

2.1 CFD Solver – GT Hybrid

The CFD simulation is carried out by an in-house solver called GT-Hybrid [25] in order to obtain the flow field data of the rotor. GT-Hybrid is a three-dimensional unsteady viscous compressible flow solver and uses the finite volume scheme. It uses a hybrid approach in obtaining the results – Navier-Stokes equations are solved in the immediate vicinity of the rotor and the Lagrangian approach is used in the far field for the vortex wake. This hybrid method greatly reduces the computational time required to model such viscous features. The current version of GT-Hybrid does not have a transition segment, as the flow is assumed turbulent everywhere.

Figure 2 shows the schematic view of the hybrid method. Close to the rotor, the viscous features are inherently captured accurately in the Navier-Stokes domain. Away from the rotor, the solver provides a "non-diffusive" modeling of the trailing vorticity as a Lagrangian free wake. As shown, a collection of piece-wise linear bound and trailing vortex elements is shed from the trailing edge of the tip of the blade and is propagated downstream into the far field. This can be accomplished by specifying the vortex-induced velocities at the boundary between the Navier-Stokes domain and the far field.

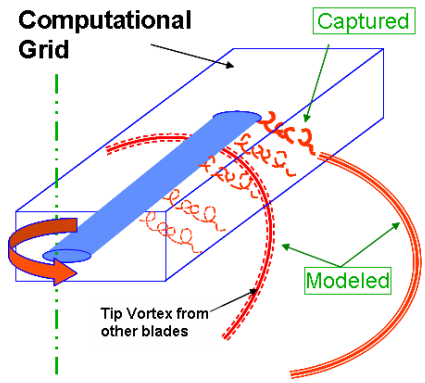

Figure 2 – Schematic view of the hybrid method.

2.2 Droplet Solver – GTDROP

The primary objective of the droplet solver, GTDROP portion of the ice accretion modeling program is to compute the local collection efficiency, β on the surface of the blade. The shape and size of the body affect the collection efficiency. The collection efficiency is a measure of the ratio of the mass flux of droplets striking the surface of the airfoil at a certain location to the mass flux of droplets in the free stream. Thus, it is a local quantity defined for a certain surface location on the airfoil body. As such, calculation of the local collection efficiency quantities utilizes the same nodes of the CFD mesh used to solve for the flow field around the blade. With the flow field as an input, there are two main methods for solving the droplet impingement on the blade surface by considering the droplet trajectory in the flow field – the Lagrangian approach and the Eulerian approach. The Lagrangian approach is an algorithm that considers the flow and convective motion of individual droplet particles and the flow field in a continuous gas phase. Implementations of the Lagrangian approach, such as the droplet solver LEWICE put forth by NASA, have become an industry standard. However, the approach used for this work is the Eulerian approach.

In general, the Eulerian approach-applied droplet impingement on a body is a two fluid model comprised of Navier-Stokes equations solved by the CFD analysis, and two additional equations for the conservation of mass and momentum related to the droplets solved by the droplet solver. Unlike the Lagrangian approach, the Eulerian approach does not track individual water droplets. Instead, it considers the average water droplet content of a control volume, called volume fraction, and averages the water droplet properties to derive momentum and mass conservation equations for each phase in the control volume.

Considering the control volume as a whole, the interaction of air particles and droplet particles can be simplified as the net drag force exerted by the mean flow on the droplets. As such, the droplet flow field must not be known for the CFD flow solver but can be treated as a passive scalar field. If the flow is known to be steady, or unchanging across time, the CFD analysis could be completed once before applying these two additional equations. However, one big advantage of the Eulerian approach over the Lagrangian approach is that it can readily be applied for dynamic flows, such as turbulent flow or when solid surfaces are in relative motion, as well.

The droplet solver makes a number of simplifying assumptions in order to linearize and discretize the governing conservation of mass and momentum equations for the droplets: i. droplets have a spherical shape, ii. droplets do not experience deformation or breaking, iii. droplets do not collide or combine, iv. heat and mass exchange with the surrounding flow is neglected, v. effect of mean flow mixing on the droplets is neglected, and vi. there are no external forces acting on the droplets except drag, gravity, and buoyancy forces.

In order to find the collection efficiency at each mesh node across time, the volume fraction, α, and droplet velocity, u_i, must be solved for by the governing conservation of mass (Equation 1) and momentum (Equation 2):

$$\frac{\partial \alpha}{\partial t} + \nabla \cdot (\alpha u_i) = 0 \tag{1}$$

$$\frac{\partial u_i}{\partial t} + u_i \cdot \nabla u_i = \frac{C_D Re_D}{24K}(u_a - u_i) + \left(1 - \frac{\rho_a}{\rho}\right)\frac{1}{Fr^2} g_i \tag{2}$$

Where u_a is the dimensionless air velocity; ρ_a and ρ are the density of air and water respectively; g_i is the gravity vector; Fr is Froude number calculated using freestream air speed and the characteristic length, typically taken to be chord length; and K is an inertia factor found using droplet diameter, d and dynamic air viscosity, μ. The basic algorithm transforms, linearizes, and discretizes these two governing equations into the computational space and finite control volume defined by the mesh for the flow field. Boundary conditions for the volume fraction and droplet velocity are defined using far field values for the freestream and using an extrapolation scheme of interior flux values for volume fraction and droplet velocity at the control volume wall. In the time dimension, an implicit time marching algorithm is employed. With this scheme, the mean flow values from the CFD solver lag the volume fraction and droplet velocity by one time step. The impingement rate that characterizes the droplet collection on the airfoil surface is the collection efficiency. This collection efficiency is a ratio of the local mass flux of water onto the airfoil surface normalized by the liquid content in the freestream and velocity of the freestream flow and is defined locally at every mesh node across time as shown as Equation 3. These collection efficiency results across the mesh and across time are fed into the ice formation and shape prediction function.

$$\beta = \frac{\alpha \rho_w u_i}{(LWC)V_\infty} \frac{A_i}{|A|} \tag{3}$$

2.3 Ice Accretion Solver – Extended Messinger Model

The ice accretion solver used for this module is an in-house program that employs the extended Messinger model. In the ice accretion process, convective heat transfer coefficients are calculated using an integral boundary layer method. Figure 3 shows the schematic of a typical ice accretion system. The substrate, or solid surface is covered by ice, *B(t)*, which is then covered by water, *h(t)* in glaze ice. The two layers have different temperatures, T and θ for ice and water, respectively. The extended Messinger model is based on the method of phase change or the Stefan condition [26, 24].

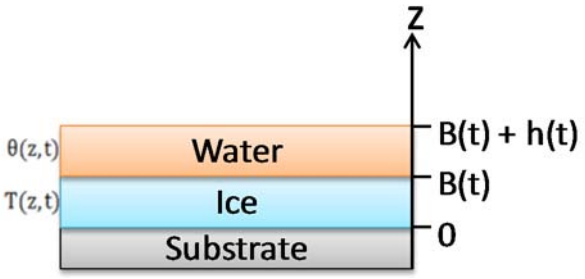

Figure 3 – Schematic of the ice and water system.

The Stefan condition entails four parts that must be solved: heat equations in the ice and water layers (Equations 4 and 5), corresponding mass balance equations (Equation 6), and a phase change or Stefan condition at the ice/water interface (Equation). In the heat equations, k is the thermal conductivity and C_p is the specific heat of the corresponding substances. The right-hand-side of Equation 6 consists of the impinging, runback, and evaporating water mass flow rate for a control volume, respectively. In Equation , L_F is the latent heat of solidification of water. Different values are used for ice density, ρ_i to account for rime or glaze ice.

$$\frac{\partial T}{\partial t} = \frac{k_i}{\rho_i C_{pi}} \frac{\partial^2 T}{\partial z^2} \tag{4}$$

$$\frac{\partial \theta}{\partial t} = \frac{k_w}{\rho_w C_{pw}} \frac{\partial^2 \theta}{\partial z^2} \tag{5}$$

$$\rho_i \frac{\partial B}{\partial t} + \rho_w \frac{\partial h}{\partial t} = (LWC)\beta V_\infty + \dot{m}_{in} - \dot{m}_{out} \tag{6}$$

$$\rho_i L_F \frac{\partial B}{\partial t} = k_i \frac{\partial T}{\partial z} - k_w \frac{\partial \theta}{\partial z} \tag{7}$$

Furthermore, for the boundary layer analysis, Thawaites' method is used for the laminar flow region, and Head's method for the turbulent flow region. The skin friction coefficient for the boundary layer and the thermodynamic analysis is obtained from the CFD simulation. The transition location is fixed at the streamwise location where the roughness Reynolds number, R_k = 600. More details can be found in Ref. [24] by Kim.

CHAPTER 3. ICE ACCRETION VALIDATION FOR SINGLE ROTOR IN FORWARD FLIGHT

The Bell Helicopter Model 206B tail rotor is used in this study to validate an ice accretion simulation for a single rotor in forward flight. The numerical simulation results are shown with the experimental results obtained from rotor blade ice tests conducted at NASA Glenn's Icing Research Tunnel (IRT) [27] in September 2013. The blade is equipped with heater blankets bonded to the blade surface. The rotor is a two-bladed teetering rotor with a pitch-flap coupling angle, δ_3 of 45 degrees, radius of 32.6 inches, and a chord of 5.3 inches. The rotor has rectangular blades with a NACA 0012 cross-section from root to tip. This section contains the methodology used for the ice accretion simulation for a single rotor in hover flight. The methodology is then validated by existing experimental data.

3.1 Method of Ice Accretion Simulation

In obtaining the GT-Hybrid flow solutions, an iterative process is taken in order to converge the blade motion, or blade flapping angle. The initial blade flapping angle is estimated using the harmonic balance approach [24]. Then GT-Hybrid is run to obtain the initial flow solutions. The sectional lift as a function of azimuth and radial location is also obtained, and the pitching and rolling moments at the hub is computed. Outputs from GT-Hybrid are fed into the blade motion calculation and is iterated until the flapping angle converges. An in-house grid generator is used to obtain a C-H grid with 131 points in the

wrap-around direction, 70 radial points, and 45 points in the normal direction, with a body fitted grid for the near field, as shown in Figure 4.

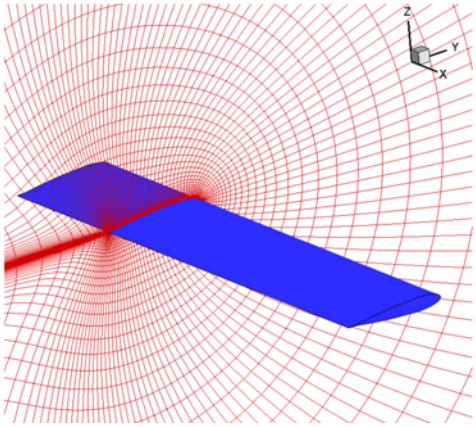

Figure 4 – 3-D blade C-H mesh for Bell tail rotor.

The CFD solution uses the Spalart-Allmaras Detached Eddy Simulation (SA-DES) turbulence model with the Roe upwind, third order accurate scheme. One of the experiment cases, Run 84, which is a dry air test for a sweep of collective pitches, is used to validate the blade motion and flow solution calculations. The conditions used for Run 84 is shown as Table 1. The five collective pitch angles were sustained for approximately 20 seconds each. Figure 5 [24] shows the experimental and computed thrust and power performance prediction for the Bell tail rotor without ice accretion. It can be seen that the coupled GT-Hybrid and blade motion analysis can produce consistent trends with the experiment.

Table 1 – Bell tail rotor Run 84 operating conditions.

Parameter	Value
V_∞ [kn]	60
T_s [°F]	14
Collective Pitch [deg]	0, 2, 5, 8, 10
Angle Sustain Time [sec]	20

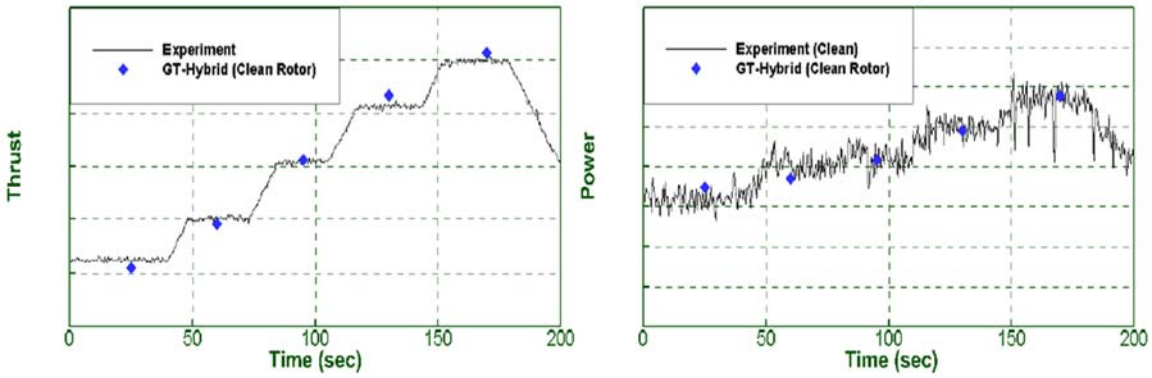

Figure 5 – Clean Bell tail rotor performance comparison for Run 83.

3.2 Validation of Ice Accretion Module

Three test cases are used to validate the ice accretion module for a single rotor in forward flight. Table 2 shows the test conditions for the Bell tail rotor for Runs 53, 54, and 83 that were used during the experiments. These test cases were chosen based on experimental ice shape availability. The results for Runs 53 and 54 are recalculated and verified with previous results [24], and Run 83 is a new case that is added in this study. In addition to the conditions listed, the LWC is 0.5 g/m^3 and the droplet MVD is 15 μm for all cases. These conditions are matched in the numerical simulations.

Table 2 – Bell tail rotor experiment test conditions for Runs 53, 54, and 83.

Run	RPM	U_∞ [kts]	T_s [°F]	Accretion Time [s]	Collective Pitch [deg]
53	1200	60	14	180	2
54	2100	60	15	60	8
83	2100	60	9	176	2

3.2.1 Run 53

As stated earlier, in order to estimate the ice shape on a blade, the blade motion is first determined. Starting with the initial estimation of the flapping angle for the clean rotor using the harmonic balance method, an iterative approach is used by coupling GT-Hybrid with a flapping dynamics analysis. The final clean rotor flow field solutions can be obtained from GT-Hybrid by using the blade motion output as one of the input files. The Eulerian droplet model is then used to calculate the droplet flow field properties, which is then fed into the Extended Messinger ice accretion solver. Within the solver, accretion of ice occurs at four azimuthal locations, ψ = 0º, 90º, 180º, and 270º. At each of these locations, the unsteady flow field data from the clean rotor is used to calculate collection efficiency.

Figure 6 shows the comparison between the clean rotor (black), experimental results (blue), and the predicted (red) ice shapes at select radial locations, r/R = 0.37, 0.49, 0.61, 0.74, 0.84, and 0.98. At inboard locations, the numerical predictions coincide greatly with the experimental data. As the spanwise location increases, the ice gradually transitions from rime ice to glaze ice due to the differences in speed that the blade sections experience. Although the current solver is unable to accurately capture the jagged features of glaze ice, the predictions agree fairly well with the average chordwise thickness of the experimental ice data. At the outboard locations, the solver seems to overpredict the ice thickness along the upper surface of the blade near the leading edge.

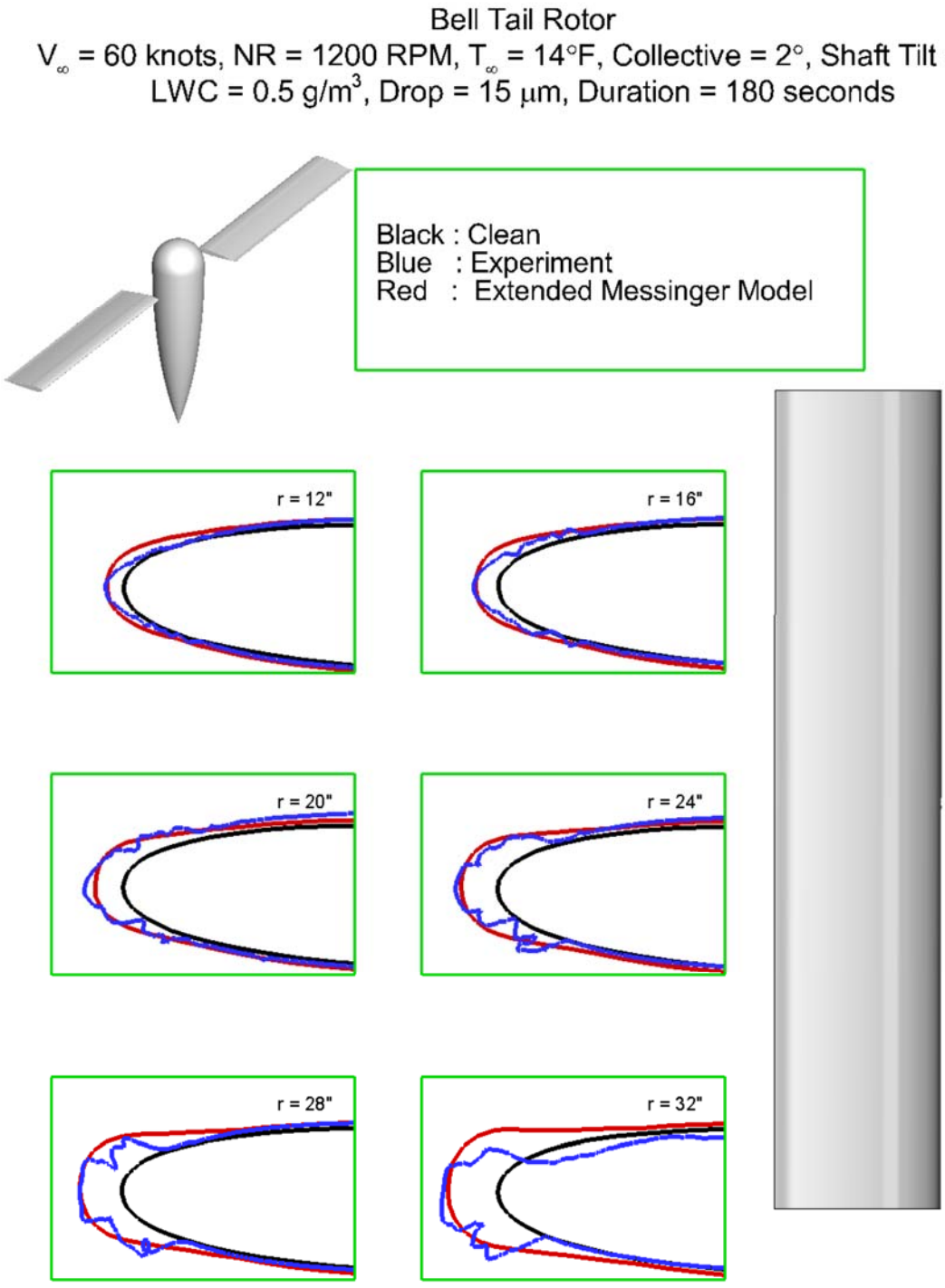

Figure 6 – Comparison of experimental and numerical ice shapes for Run 53.

3.2.2 Run 54

As shown in the table above, for Rum 54, the rotor RPM is significantly higher at 2100, compared to 1200 for Run 53. Additionally, the accretion time for Run 54 is shorter and the collective pitch angle is higher compared to Run 53. All other parameters are unchanged or vary only slightly. Since the RPM is high for Run 54, the kinetic heating effect must be considered. This is done by turning on the option to read the surface temperature from GT-Hybrid in the Python script used for ice accretion. There are no additional changes in the solution approach from Run 53.

Figure 7 shows the comparison of the experimental and numerical ice shapes for Run 54 at the same six radial locations as Run 53. Similar to Run 53, the experimental and numerical results show great agreement at the inboard locations. The effects of kinetic heating can be seen starting at the midboard locations, as the ice shape is less glaze compared to the corresponding shapes for Run 53 – the heating prevents the ice from growing. The ice accretion solver is able to correctly take into account the surface temperature effects, and thus the prediction shows good agreement with actual results. Without accounting for the surface temperature the predicted ice shape will be significantly thicker at the leading edge. At outboard locations, the solver is unable to capture the smaller details of glaze ice especially along the lower surface of the leading edge. However, the predicted general maximum thickness coincides fairly accurately for those locations.

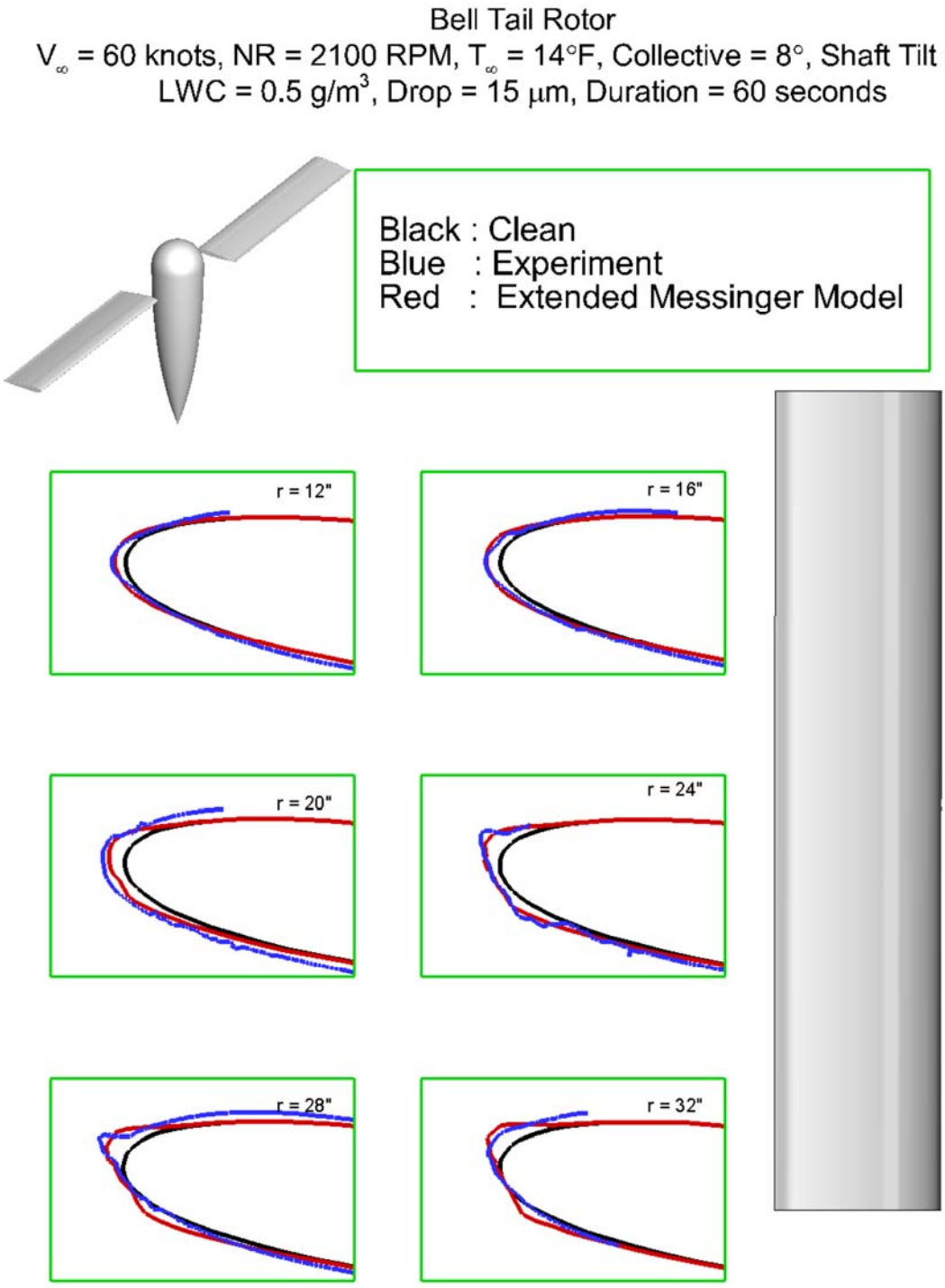

Figure 7 – Comparison of experimental and numerical ice shapes for Run 54.

3.2.3 Run 83

Run 83 is a new case added to the validation of the ice accretion solver. The conditions are similar to Run 53, other than that the RPM is significantly high at 2100 and the static temperature is slightly lower at 9 ºF for Run 83. Similar to Run 53, kinetic heating effects are taken into account due to the high RPM. All of the other approach methods are identical to Run 53.

Figure 8 shows the comparison of experimental and numerical ice shapes for Run 83 at r/R = 0.31, 0.34, 0.58, 0.61, and 0.77. These locations are chosen based on the availability of experimental data obtained at the IRT [28]. The predicted ice shape without experimental results is shown at r/R = 0.98 for reference. Similar to the other two cases, the experimental and numerical results agree well for the inboard locations. At midboard and outboard locations, the ice shape is highly glaze despite the high RPM. This results from the decrease in static temperature. The solver does predict the maximum thickness well for the midboard locations but overpredicts at the upper and lower surfaces and is not capable of capturing the multiple ice horn tips.

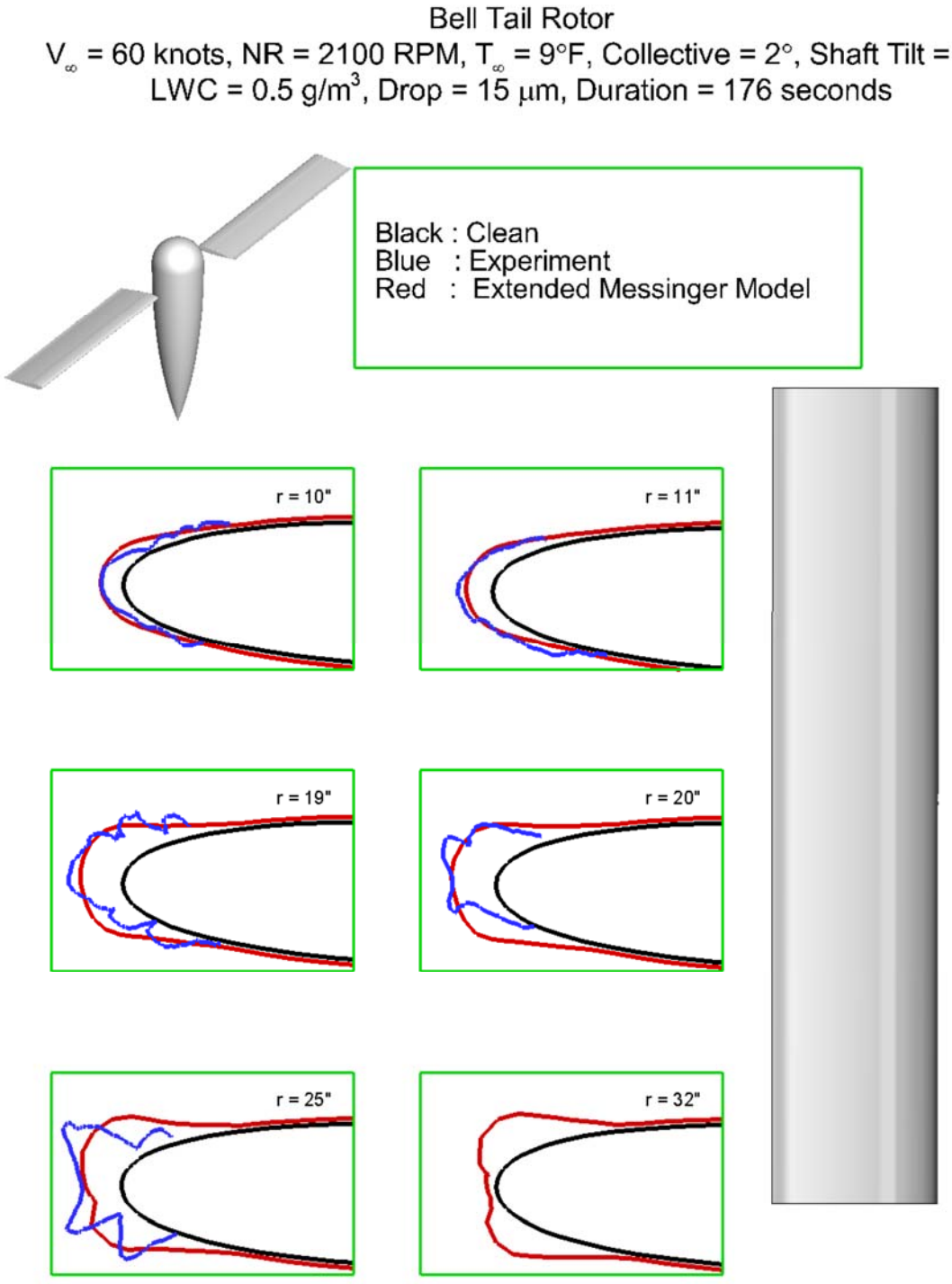

Figure 8 – Comparison of experimental and numerical ice shapes for Run 83.

CHAPTER 4. ICE ACCRETION SIMULATION FOR COAXIAL ROTOR IN HOVER

A coaxial rotor configuration tested by Harrington [19] is modeled in this study. Harrington performed static thrust performance experiments at the full-scale wind tunnel at NASA Langley in 1951 for two coaxial rotor configurations, Rotor 1 and Rotor 2 in hover. In this study, Rotor 2 is modeled and its specifications are shown as Table 3. The blades on the Rotor 2 is of all-metal construction, have a constant chord from root to tip and are untwisted. The thickness to chord ratio varies linearly with NACA 0028 at the root cutout (20% of R) and NACA 0015 at the tip (100% of R).

Table 3 – Harrington Rotor 2 geometry.

Parameter	Value
Number of Rotors	2
Number of Blades	2
D [ft]	25
h/D [ft]	2 (8% of D)
Root Cutout [%]	20% of R
Chord [ft]	1.5
$\sigma_{\text{single rotor}}$	0.076
$\sigma_{\text{coaxial rotor}}$	0.152
Airfoil	NACA 0028/0015 (root/tip)
Twist	Untwisted
Shaft Tilt [deg]	0

The in-house ice accretion model discussed in the previous chapter is adapted for application to a coaxial rotor configuration. In order to validate the flow solution, performance analysis is completed for the Harrington Rotor 2 in hover in the absence of

ice accretion. Then, ice shape is calculated for the same rotor for three collective pitch angles, Case 1, Case 2, and Case 3. Finally, the performance degradation of the coaxial rotor due to ice is estimated.

4.1 Clean Rotor Performance Prediction

Harrington conducted static-thrust experiments with Rotor 2 for two tip velocities, V_{tip} of 327 ft/s and 392 ft/s and for a range of collective pitch angles. In this study, the latter and larger tip velocity is used. The simulations are performed for Rotor 2 in hover, and the blades are assumed to be rigid in flapping motion as well as in the plane of rotation, its only motion being the rotation about the hub center. An in-house grid generator is used to obtain a C-H grid with 131 points in the wrap-around direction, 70 radial points, and 45 points in the normal direction, with a body fitted grid for the near field. The grid is shown as Figure 9. The flow field data is obtained for Rotor 2 using GT-Hybrid for varying collective pitch angles of 2 to 12 degrees in 1-degree increments. Within the GT-Hybrid analysis, the collective pitch of the lower rotor is adjusted so that the net torque on the upper and lower rotors is balanced to zero. The simulations are performed on a Linux cluster with 12 CPU cores in approximately 36 hours per collective pitch setting.

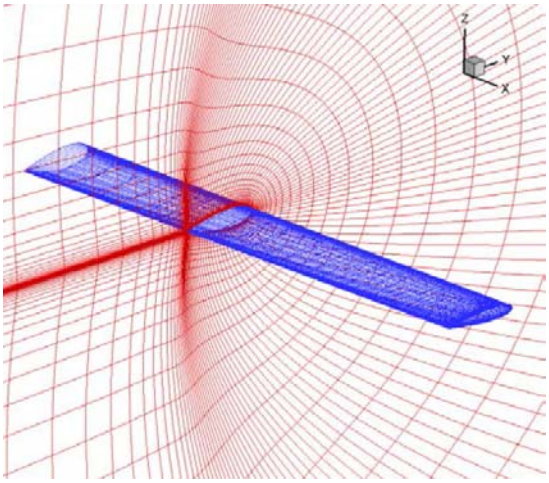

Figure 9 – 3-D blade C-H mesh for Harrington Rotor 2.

Simulations on Star-CCM+ were performed for collective pitch angles of 2, 4, and 6 degrees for 8 to 10 rotor revolutions each for a converged data. A time step of 1-degree azimuth angle was used with 10 to 15 sub-iterations per time step. The experimental and numerical performance results are shown as Figure 10. The results are in good agreement for low to moderate thrust settings, but GT-Hybrid results slightly underestimate the FM at lower thrust settings and overestimates the FM at higher settings. Star-CCM+ results agree better with the experiment at the higher thrust settings. Figure 11 shows the contributions of the upper and lower rotors to the overall thrust and associated FM. The linear relationship in the left figure shows that the calculated thrust between the upper and lower rotors are not affected by the required thrust. The right figure shows that the upper rotor has high FM for both analysis methods, which is an expected result due to equal power from the trimmed rotor. More performance results and detail can be found in the author's previously published paper [29] attached to this document as Appendix A.

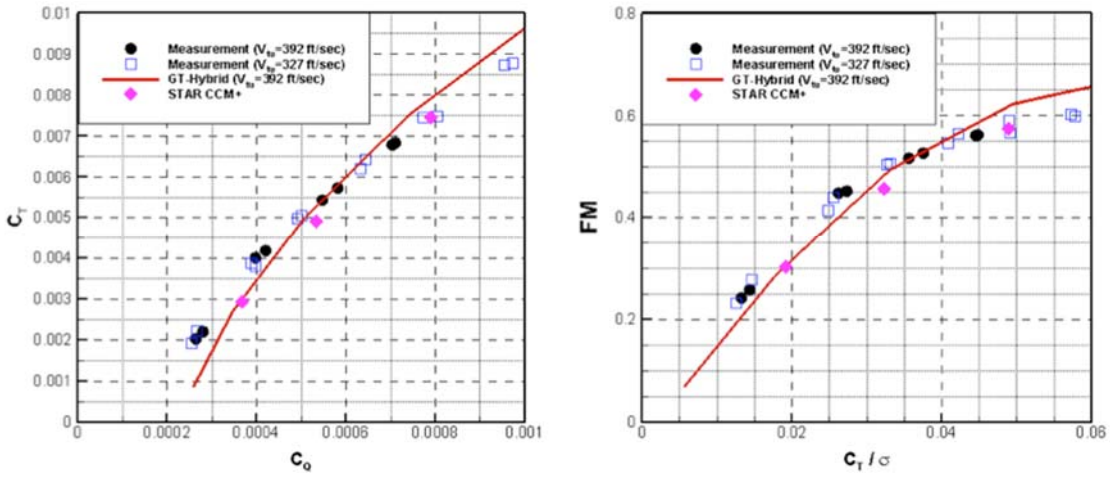

Figure 10 – Hover performance of the Harrington Rotor 2.

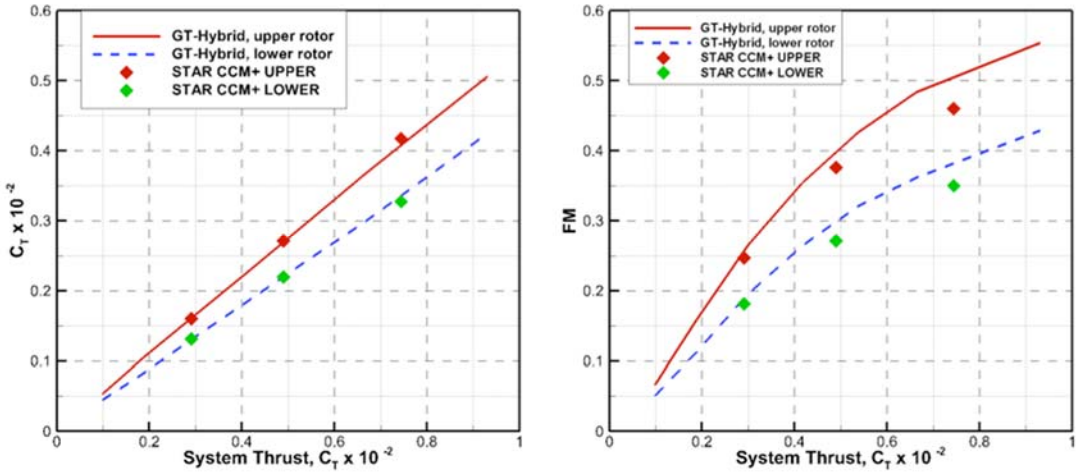

Figure 11 – Contributions of the upper and lower rotors to overall thrust and associated figures of merit.

Important to the ice accretion modeling environment is the flow field solution that is fed into the droplet solver and the ice accretion simulator. The predicted velocity field is critical to estimating the performance of the clean rotor and modeling collection efficiency over the blade surfaces. Figure 12 is a visualization of the downwash across the upper rotor disc and lower rotor disc at 2 degree collective pitch angle. It shows the predicted increase of downwash with span location for each rotor. It also shows that the downwash is predicted to be greater at any given location for the lower rotor compared to the upper rotor

because each rotor is inducing velocity. At the tip region of both rotors, the effect of predicted vortex shedding can be seen as a sharp drop off in downwash. Figure 13 shows the surface temperature across the upper and lower rotor blades at the 2 degree collective pitch angle setting. The plot shows that temperatures generally increase spanwise along the blade and there is a region of higher temperatures along the leading edges. The surface temperature distribution plays a role in the heat transfer analysis with in the ice accretion simulation module.

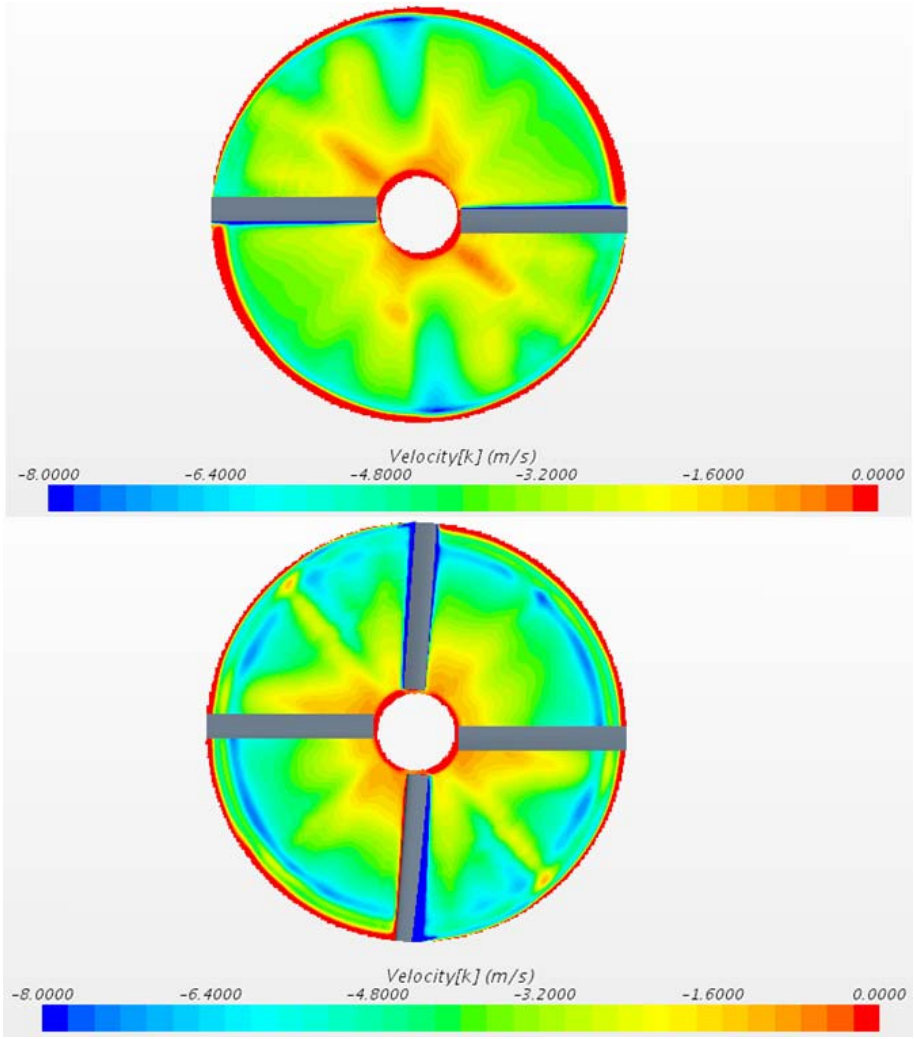

Figure 12 – Clean rotor downwash across upper rotor disc (top) and lower rotor disc (bottom) at 2 degree collective pitch angle.

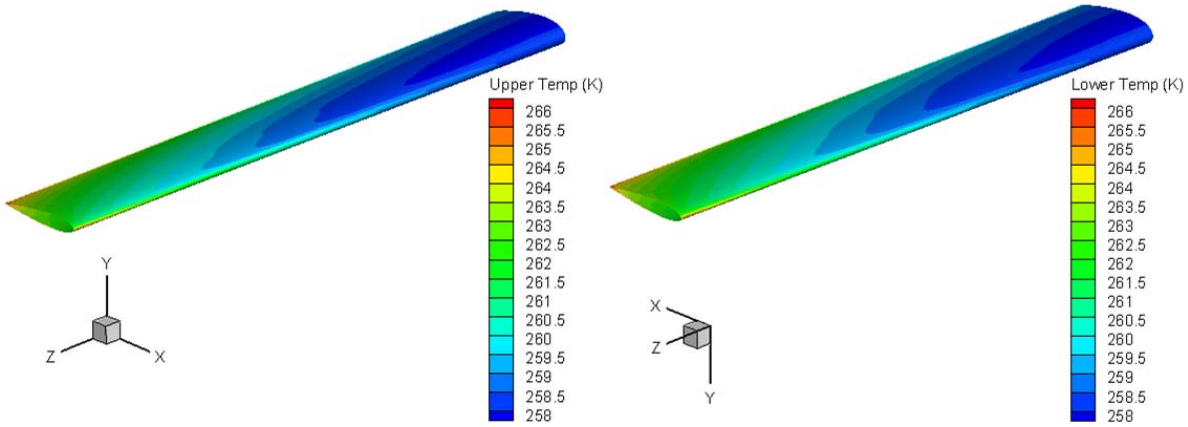

Figure 13 – Blade surface temperature distribution for upper and lower rotor at 2 degree collective pitch angle.

4.2 Collection Efficiency Prediction

As ice accretion modeling has previously not been done for a coaxial rotor, this section will discuss the intermediate results for collection efficiency, β. Collection efficiency alone does not explain the ice accretion phenomenon because thermodynamic processes must be considered. However, collection efficiency is a critical aerodynamics result because it describes the amount and location of water impingement on the blade surfaces. Coaxial rotor impingement of water droplets on each blade surface is dependent on the flow field solution, which reflects modeling of the complex interactions between the upper and lower blades.

The top panels in Figure 14 show a contour plot of the predicted collection efficiency distribution across the upper and lower rotor blade surfaces for the Case 3 simulation with 6 degree collective pitch angle. Similar to a single rotor configuration, the region of highest collection efficiency is concentrated near the leading edges of each blade and the height of

the peak value generally increases in the spanwise direction as the airspeed increases. The six panels below the contour plots show the predicted 2D collection efficiency distribution at select radial locations. For each spanwise location, the horizontal axis represents the dimensionless location on the 2D airfoil surface, which follows the upper surface an airfoil from trailing edge (x = -1) to leading edge (x = 0) and back to the trailing edge (x = 1) along the bottom surface. In general, it can be seen that the predicted collection efficiency distributions are very similar for the upper and lower rotor blade at each location. Both distributions are shifted modestly in the positive direction (toward the trailing edge along the bottom surface) as a result of the angle of attack. However, compared to the upper rotor blade, the predicted collection efficiency distribution on the lower rotor blade is slightly higher on the leading edge region at each of the spanwise locations, a characteristic that becomes more prominent at the outboard locations. This may be the effect of the downwash velocity induced by the upper rotor blade on the trajectory of droplets approaching the lower rotor blade.

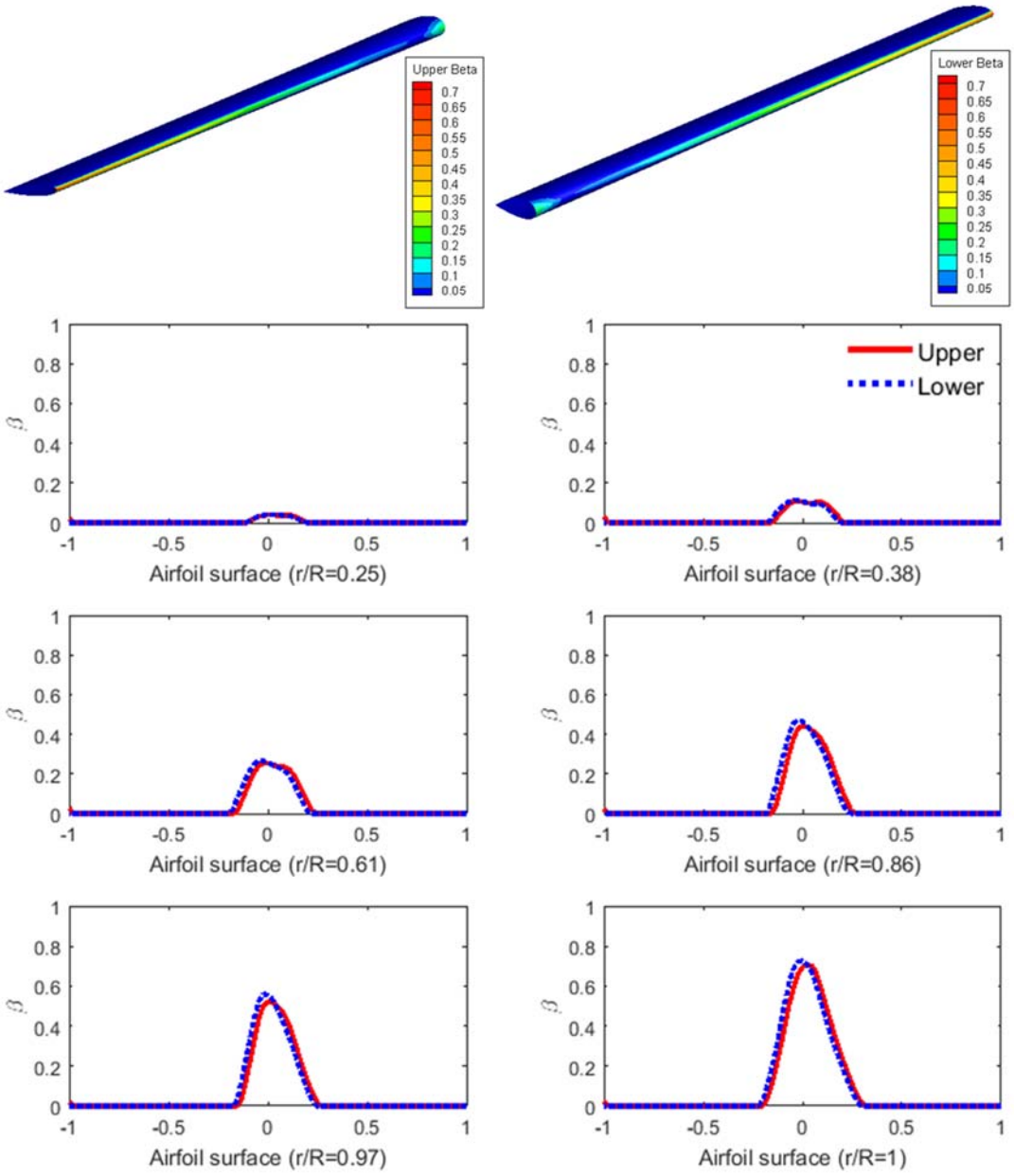

Figure 14 – Collection efficiency distribution for upper and lower rotor.

The concentration thus far was on the results for Case 3 because this case provided the most prominent results for the above discussion. To get an idea of how the collective pitch angle affects the collection efficiency, the peak collection efficiency at each radial location for the upper and lower rotor blades was plotted for Case 1, Case 2, and Case 3 in Figure 15, Figure 16, and Figure 17, respectively. These plots more clearly depict the

observations that can be made from the sectional panels in Figure 14. For each case, it can be seen that the predicted peak collection efficiency for the lower rotor blade lies above that of the upper rotor blade at every location and the magnitude of the difference generally grows with radial location. Inboard of approximately 75% span, the differences between the lower and upper rotor blade are negligible. The predicted differences by varying collective pitch is most easily seen at the outboard region (>75% span), where the deviation between the lower and upper rotor blade peak values seems to increase with collective pitch angle. However, even for Case 3, the difference between the lower and upper rotor blade peak collection efficiency values remains less than 5%. The predicted impact of collective pitch on peak collection efficiency may be attributable to the changing magnitude of downwash and any unsteady affects induced by the upper blade over the lower blade. For each of the collective pitch cases, a sharp increase in collection efficiency is predicted in the region closest to the tip and is potentially attributable to tip vortices. A slightly higher peak collection efficiency is also predicted near the blade root across all cases, but the location and magnitude make it unlikely to have significant impact on performance predictions.

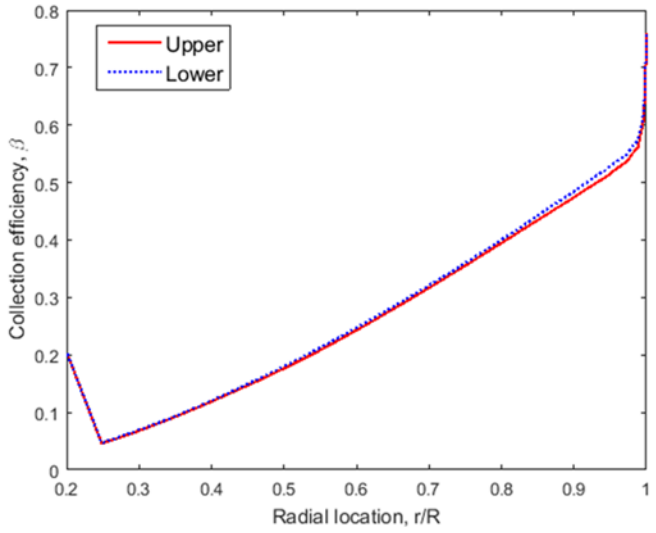

Figure 15 – Maximum collection efficiency by radial location, Case 1 (2 degree collective pitch angle).

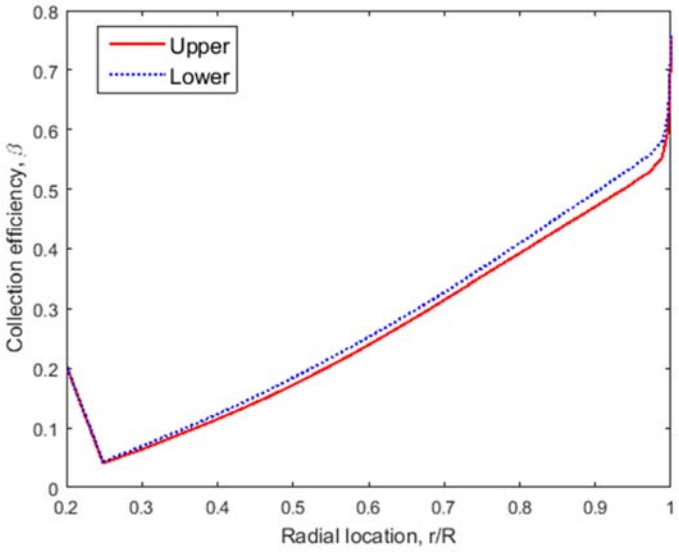

Figure 16 – Maximum collection efficiency by radial location, Case 2 (4 degree collective pitch angle).

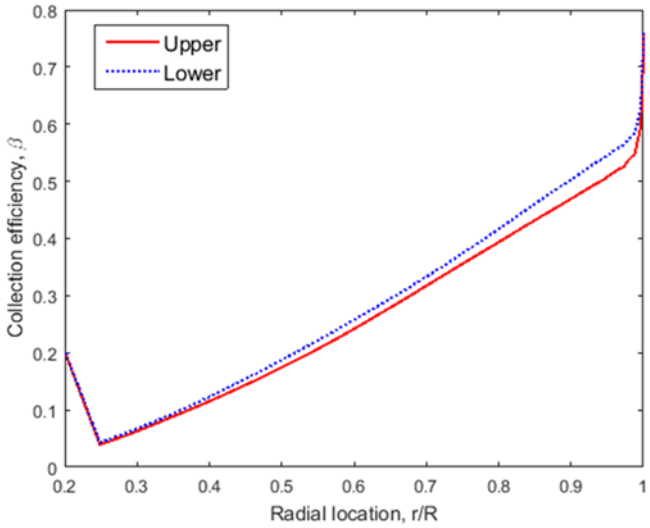

Figure 17 – Maximum collection efficiency by radial location, Case 3 (6 degree collective pitch angle).

4.3 Ice Shape Prediction

The ice accretion is predicted for Rotor 2 for three cases. While experimental ice accretion studies for single rotors have been conducted extensively, similar studies for contra rotating coaxial rotors have not been done to the author's knowledge. Therefore, comparison or validation of simulations with experimental results is not yet possible and will be left to future research. As discussed in the numerical formulation, the ice accretion module essentially uses the collection efficiency information output from the droplet solver to simulate droplets colleting on the blade surfaces and numerically solves heat and mass transfer equations to predict the formation of ice. This simulation and its results are discussed in this section.

4.3.1 Simulation Parameters

Table 4 summarizes the key parameters of the operating condition for the simulation of ice accretion of the coaxial rotor. Most of these values were chosen using the Bell tail rotor simulation discussed in Chapter 3 as a baseline. However, the tip speed of 392 ft/s (or 299 RPM) is taken from the experiments conducted by Harrington. Since this value is significantly lower compared to the icing conditions for the Bell tail rotor, the duration of the ice accretion simulation is increased to 300 seconds to compensate. Additionally, due to the low RPM, kinetic heating effects can be ignored in this coaxial case, unlike Runs 54 and 83 from the Bell tail rotor case.

Table 4 – Icing operating conditions for the coaxial rotor.

Parameter	Value
V_∞ [ft/s]	0
V_{tip} [ft/s]	392
LWC [g/m^3]	0.5
Droplet Diameter [μm]	15
T_s [°F]	14
Accretion Time [sec]	300

4.3.2 Case 1

The ice shape is calculated for the modeled Rotor 2 with the icing operating conditions listed above with a collective pitch of 2 degrees for both the upper and lower rotors. Figure 20 shows the sectional view of the clean rotor (black), upper rotor ice shape (red), and lower rotor ice shape (blue) overlaid at select radial locations, r/R = 0.25, 0.38, 0.61, 0.86, 0.97, and 1.0. It can be seen that the predicted ice is rime throughout the span

of the blade as there are no spikes or horns in the ice shape, which are characteristics of glaze ice. In general, the thickness of the predicted ice at any location on a given section increases with the radial distance along the blade as airspeed increases. Comparing the ice shape on the upper and lower rotor blade at any given radial location, it can be seen that the differences for the given rotor geometry and operating conditions are modest. Upon close inspection one can observe that the lower rotor blade ice is predicted to form slightly higher on the leading edge compared to the upper rotor, particularly at the outboard locations. This result is consistent with the predicted collection efficiency results and a higher downwash over the lower rotor blade to the interaction with the upper rotor blade.

Figure 18 shows the predicted maximum ice thickness of the upper and lower rotor blades across all radial locations. Figure 19 shows the cross sectional area of the predicted ice for the upper and lower rotor blades across all radial locations. The overall trend for both maximum ice thickness and ice cross sectional area are similar to the fairly linear, positive trend predicted for maximum collection efficiency, in Figure 15, at inboard locations. However, beyond $r/R \approx 0.8$, both of these predicted metrics of ice shape begin to level off, where collection efficiency did not. Because collection efficiency was an aerodynamics result and ice formation includes the heat transfer processes, the leveling trend in thickness and area may be related to the predicted increasing blade surface temperatures with radial location seen from the flow field solution in Figure 13. The predicted ice area sharply increases near the tip (beyond $r/R \approx 0.99$) in line with the collection efficiency. The maximum ice thickness predictions vary from 0 in. to approximately 0.28 in. As was discussed for the ice shape plots, the differences in ice thickness and area distribution for the upper and lower rotor blade are modest, so the

quantity of ice predicted to accrete on each blade does not differ significantly. Beyond *r/R* ≈ 0.8, the maximum thickness of the ice on the lower rotor is on average 1% greater than that of the upper rotor. The maximum difference in ice area between the upper and lower is 5% at the tip.

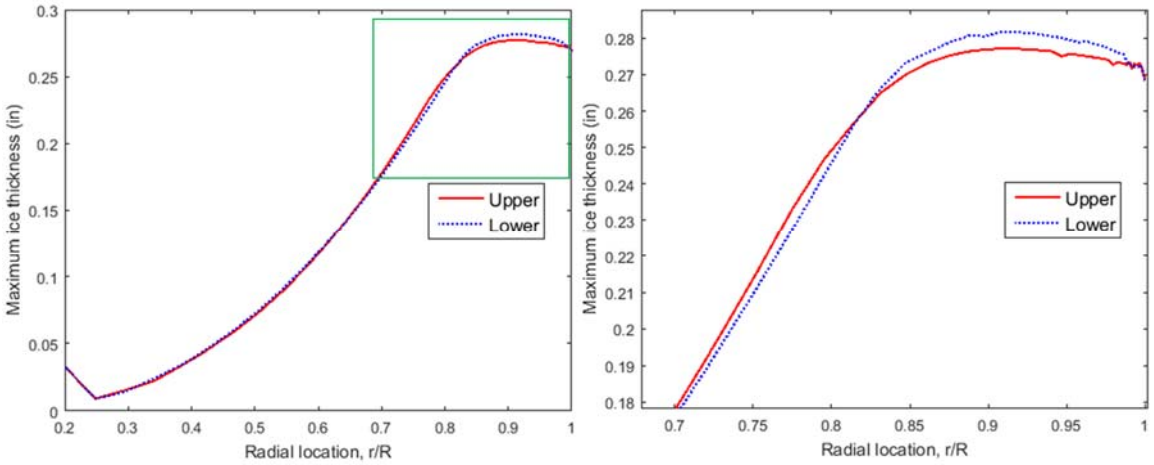

Figure 18 – Maximum ice thickness of upper and lower rotor along radial location at collective pitch of 2 degrees.

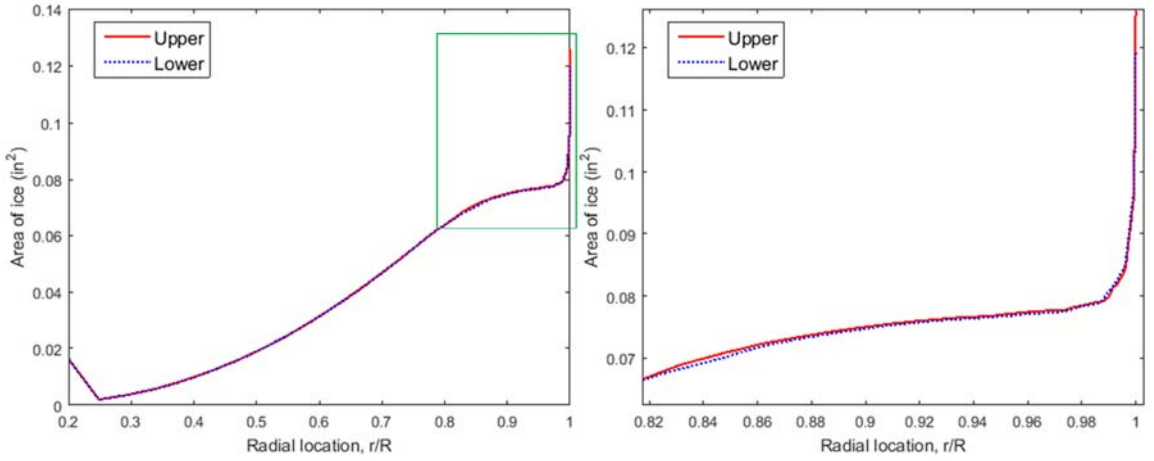

Figure 19 – Total area of ice of upper and lower rotor at different cross-sections along radial location at collective pitch of 2 degrees.

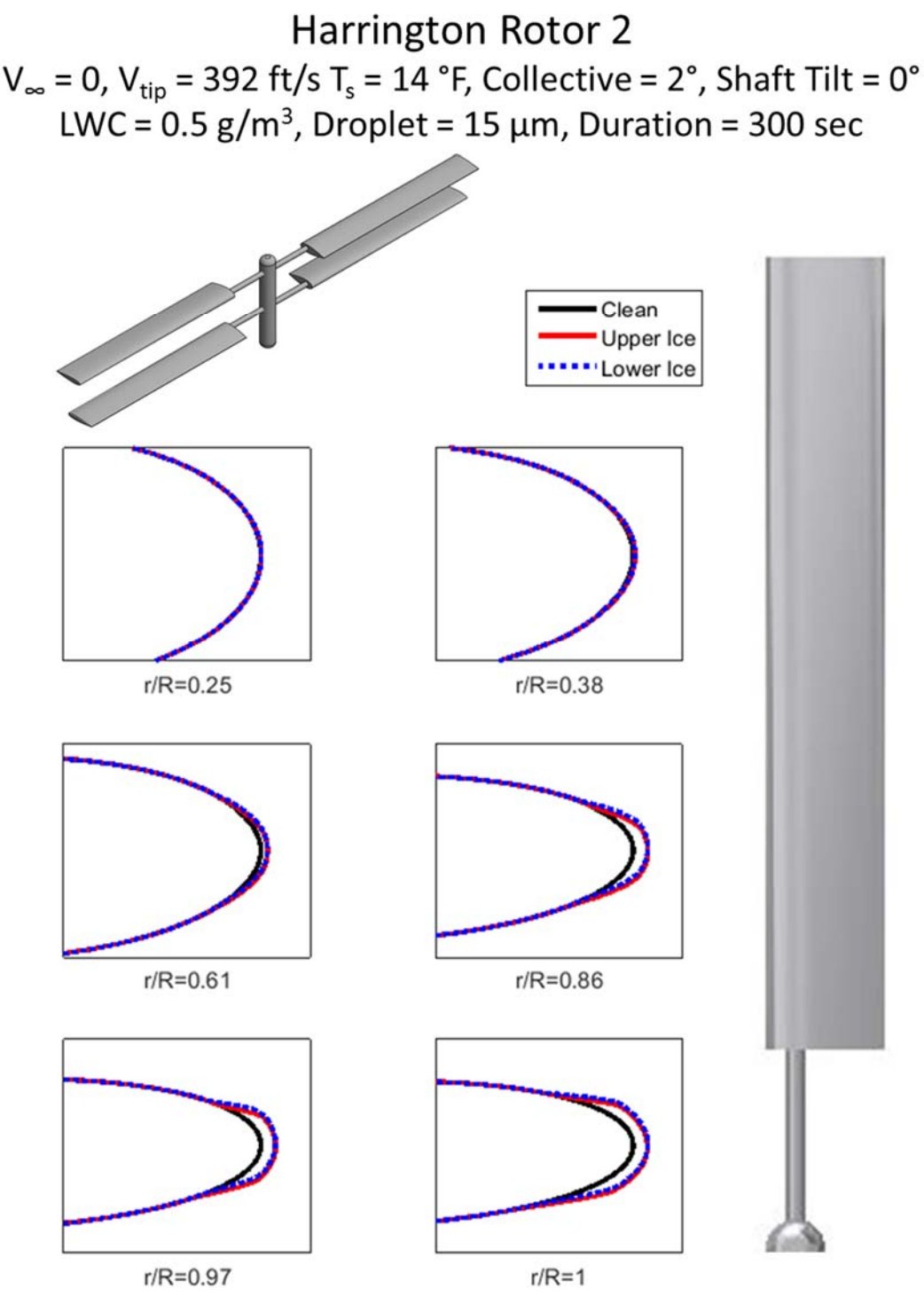

Figure 20 – Comparison of the upper and lower ice shapes for Harrington Rotor 2 with collective pitch of 2 degrees.

4.3.3 Case 2 and Case 3

Figure 23 and Figure 24 show the predicted ice shape for the upper and lower rotor blade at select span locations for Case 2 (with 4 degree collective pitch angle) and Case 3 (with 6 degree collective pitch angle), respectively. The corresponding plots for maximum ice thickness and cross sectional ice area are given in Figure 21 and Figure 22 for Case 2 and Figure 25 and Figure 26 for Case 3, respectively. Only minor difference to the predicted ice accretion results obtained for Case 1 are observed. As a result, most of the Case 1 discussion of the results, in terms of ice shape, ice quantity, comparison of spanwise trends, and comparison of upper and lower rotor blades, can be applied to Case 2 and Case 3. Thus, only the differences between the cases are elaborated.

A slight difference in ice shape across the three cases is observable at the three most outboard locations (r/R = 0.86, 0.97, 1). At these locations, one can see that ice is predicted to accrete lower on the leading edge due to the increase in collective pitch angle. Another difference in the predicted ice shape can be deduced from the maximum thickness plots. Comparing the plots across the cases, the most noticeable difference occurs at the outboard region (beyond $r/R \approx 0.8$). In this region, the maximum thickness of the lower rotor blade is an average of 1.1%, 4.6%, and 6.4% larger compared to the upper rotor blade for Case 1, Case 2, and Case 3, respectively. Further analysis of this region, shows that the increasing deviation of the average maximum thickness between the upper and lower rotor blade is a result of both an increasing average maximum ice thickness in the lower blade and a slight decrease in average maximum thickness for the upper blade as collective pitch increases. Comparing the cross sectional are for the predicted ice shape over the same outboard region shows that ice area on the lower blade increases relative to that of the upper

blade as collective pitch increases. Across this outboard region, the lower blade had an average of 0.5% less ice area for Case 1 and 1.0% and 2.8% larger average ice area for Case 2 and Case 3, respectively, compared to the upper blade area. Comparing the plots one can see that the overall magnitudes of the ice cross sectional areas were not affected significantly by the collective pitch differences between the three cases tested.

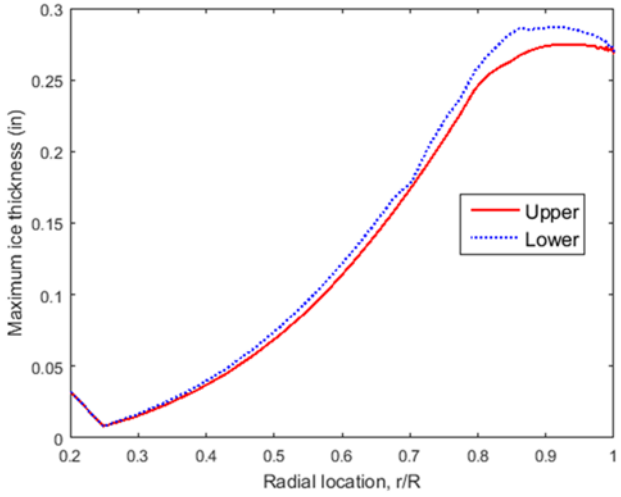

Figure 21 – Maximum ice thickness of upper and lower rotor along radial location at collective pitch of 4 degrees.

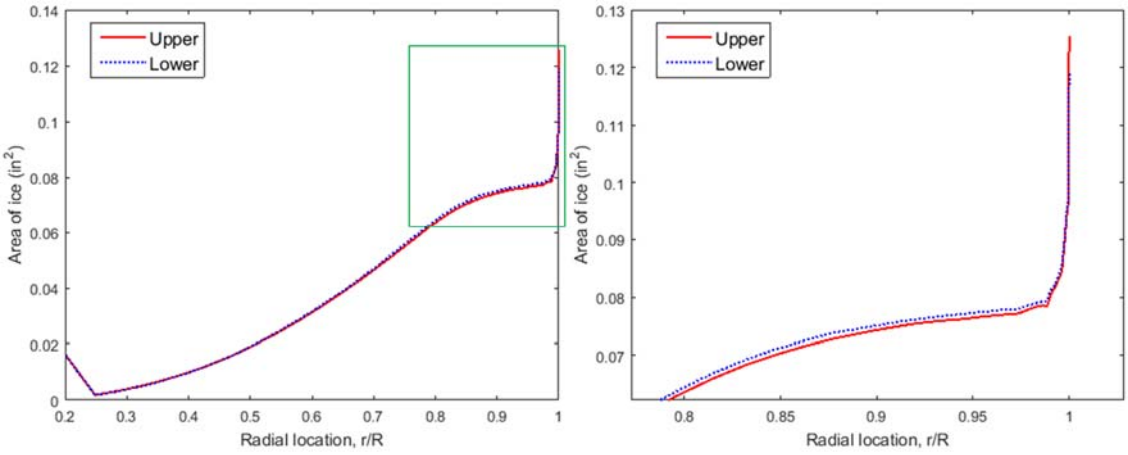

Figure 22 – Total area of ice of upper and lower rotor at different cross-sections along radial location at collective pitch of 4 degrees.

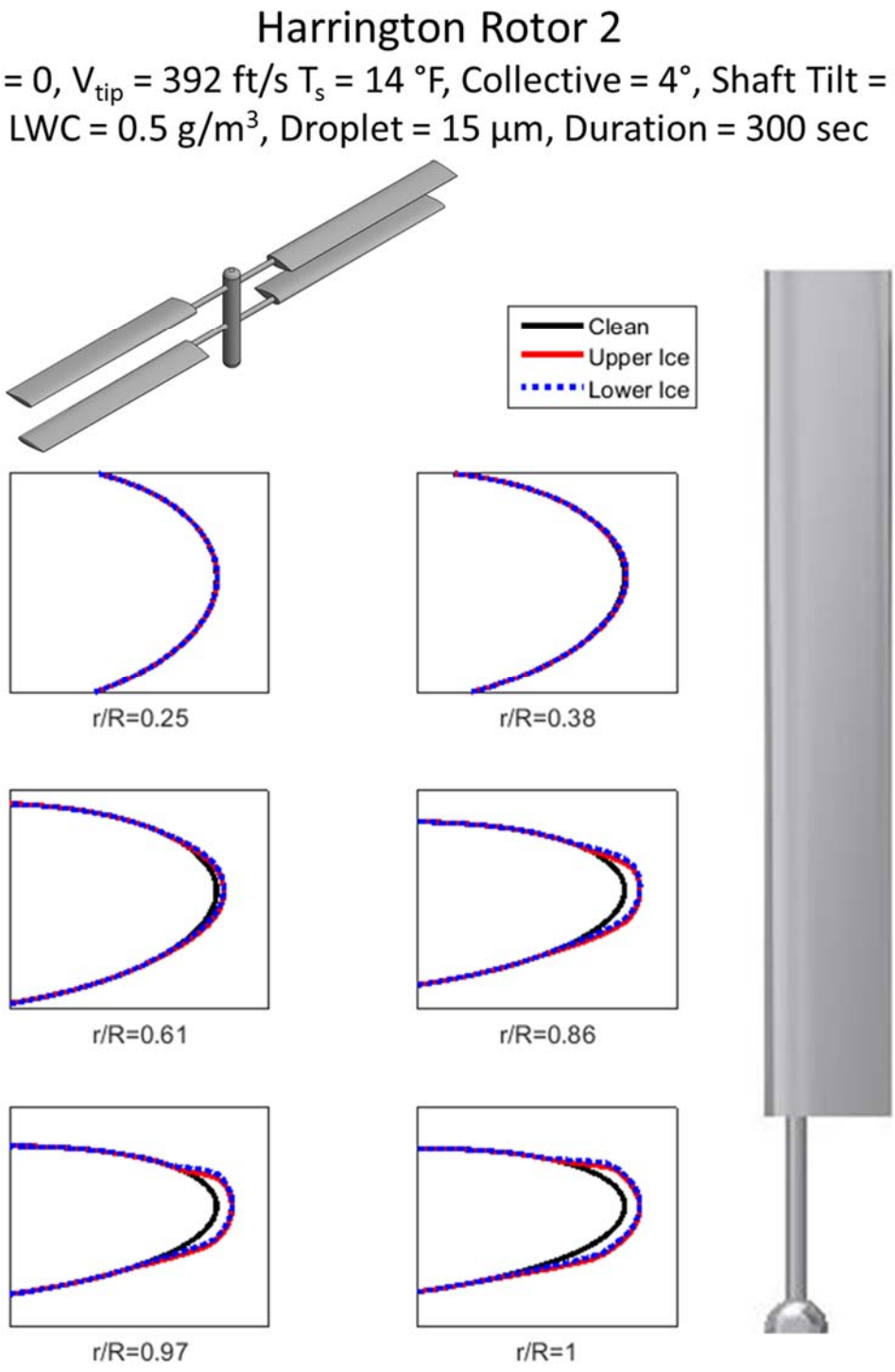

Figure 23 – Comparison of the upper and lower ice shapes for Harrington Rotor 2 with collective pitch of 4 degrees.

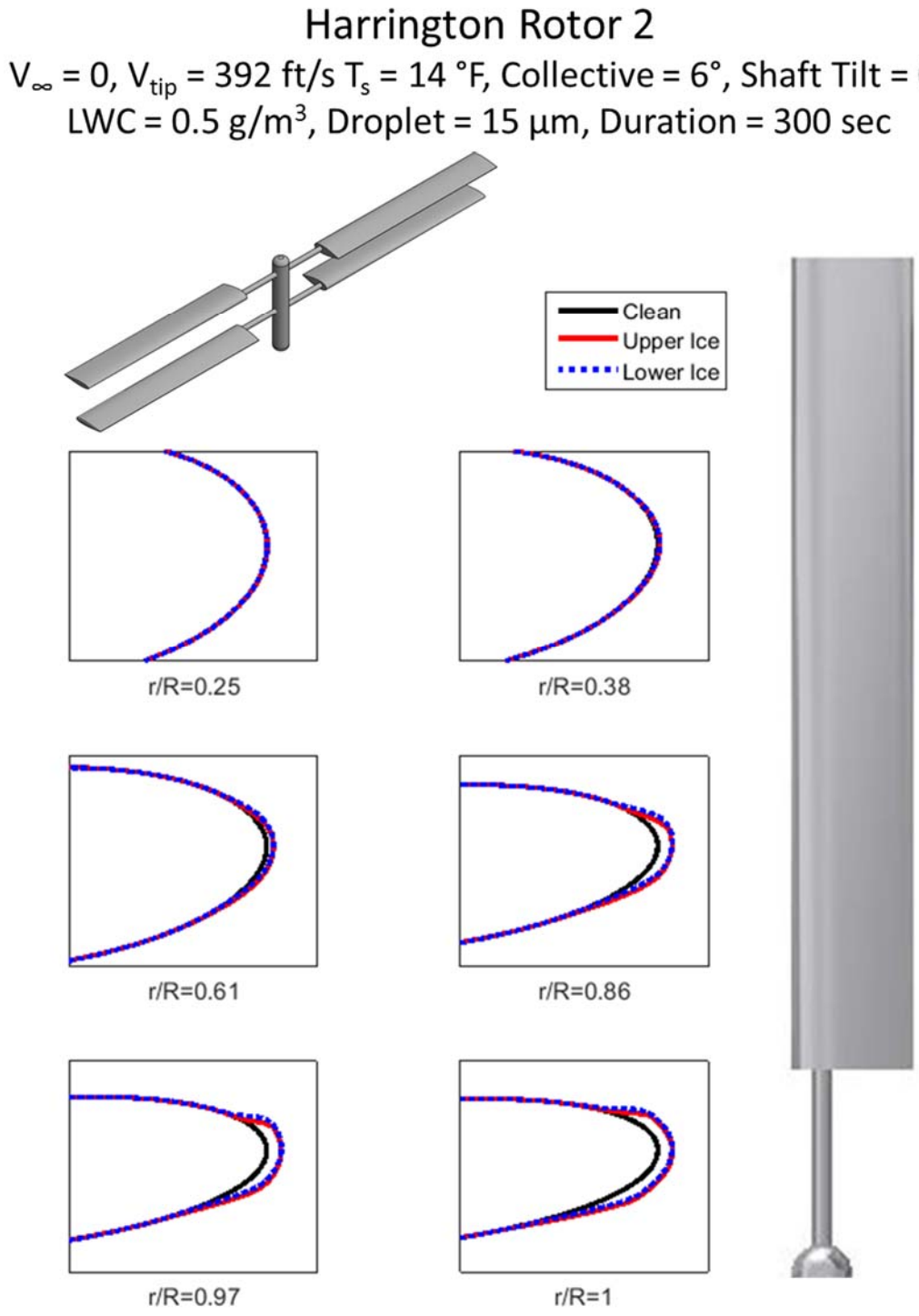

Figure 24 – Comparison of the upper and lower ice shapes for Harrington Rotor 2 with collective pitch of 6 degrees.

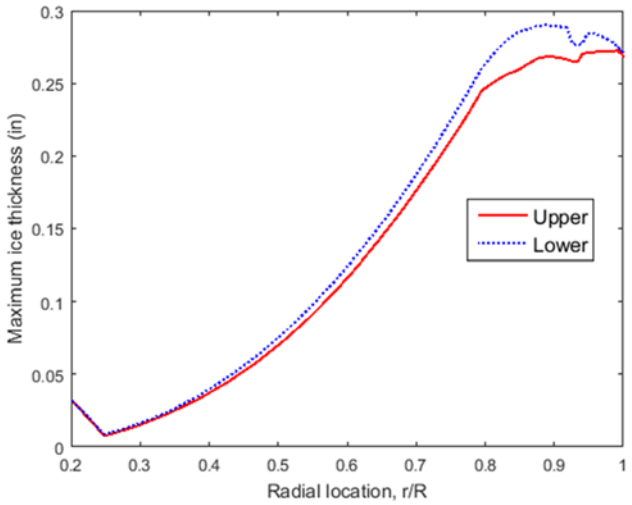

Figure 25 – Maximum ice thickness of upper and lower rotor along radial location at collective pitch of 6 degrees.

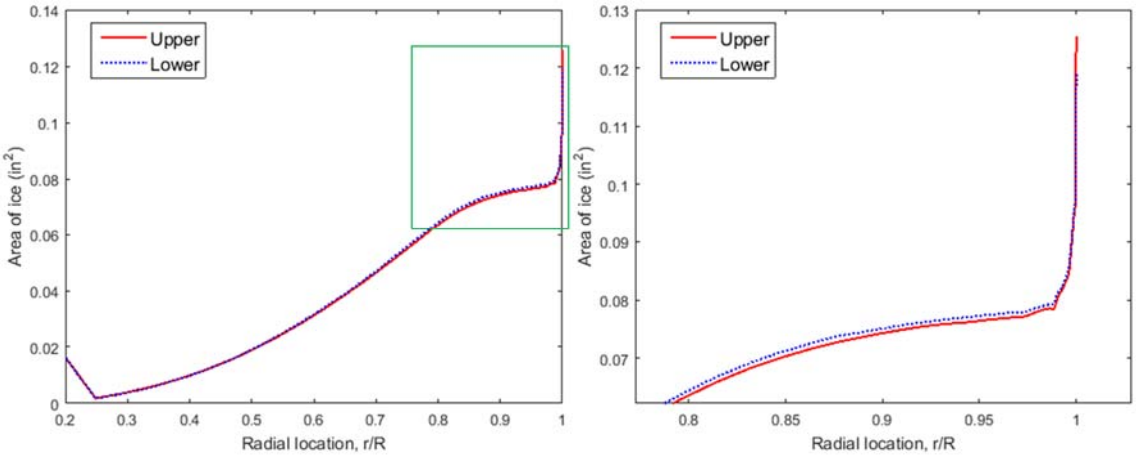

Figure 26 – Total area of ice of upper and lower rotor at different cross-sections along radial location at collective pitch of 6 degrees.

4.4 Degraded Performance Prediction

Upon obtaining iced section geometries for the upper and lower coaxial blades, the performance analysis is repeated using the in-house icing approach discussed in Chapter 2. The 2-D iced blade sections is used to create 3-D blade geometry, which is then re-meshed using the in-house grid generator. Then GT-Hybrid is used to analyze the performance degradation of the iced rotor. Figure 27 shows the vorticity contour using the wake-

capturing analysis of the iced coaxial rotor at a collective pitch of 6 degrees, after the starting vortices are shed downward. Due to the hover condition and low RPM, the downward inflow was also very small, and the vortex shedding was not seen until after approximately 6 revolutions. In the performance degradation analysis presented below, GT-Hybrid was solely used, and Star-CCM+ wake-capturing analysis was not, due to limitations in computational power.

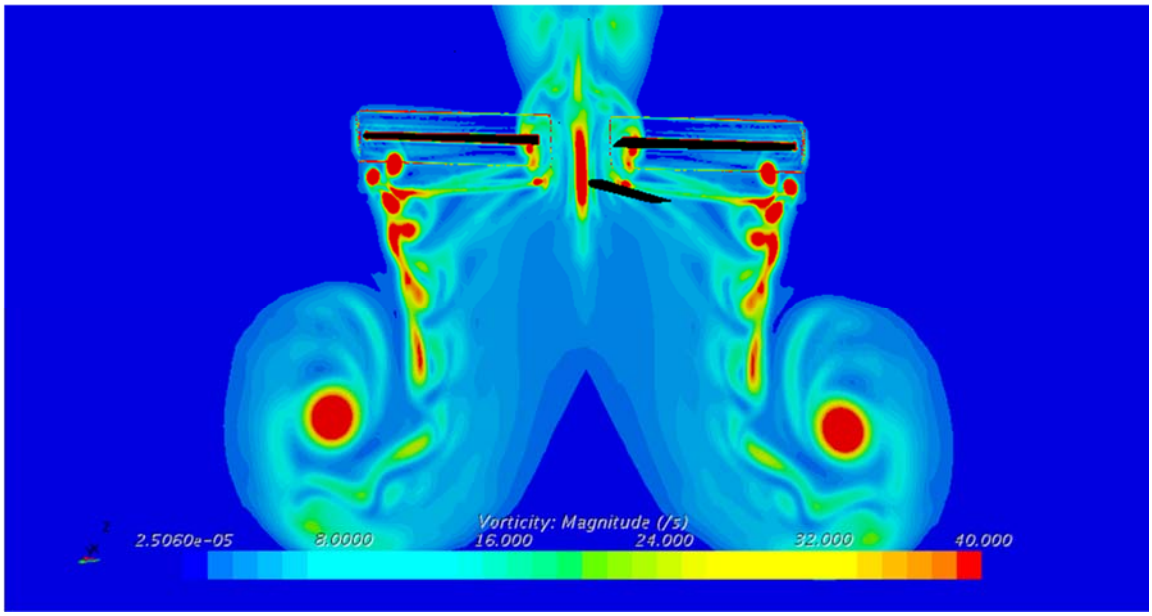

Figure 27 – Vorticity contour of iced coaxial rotor at collective pitch of 6 degrees after the starting vortices are shed downward.

Figure 28 shows the thrust coefficient plotted against the power coefficient for the coaxial rotor. The iced performance thrust curve lies below the clean configuration for all thrust settings. At low power settings, ($C_Q \approx 0.0003$) the iced rotor has a 38% decrease in thrust. At high settings ($C_Q \approx 0.0009$), the iced rotor has about a 4% decrease in thrust. The percentage difference decreases as the power settings are increased. As seen in the clean rotor performance prediction section, the GT-Hybrid analysis tends to overpredict the

performance at higher thrust settings. Therefore, the thrust to power curve may be assumed to have a lower slope when the wake-capturing method is used.

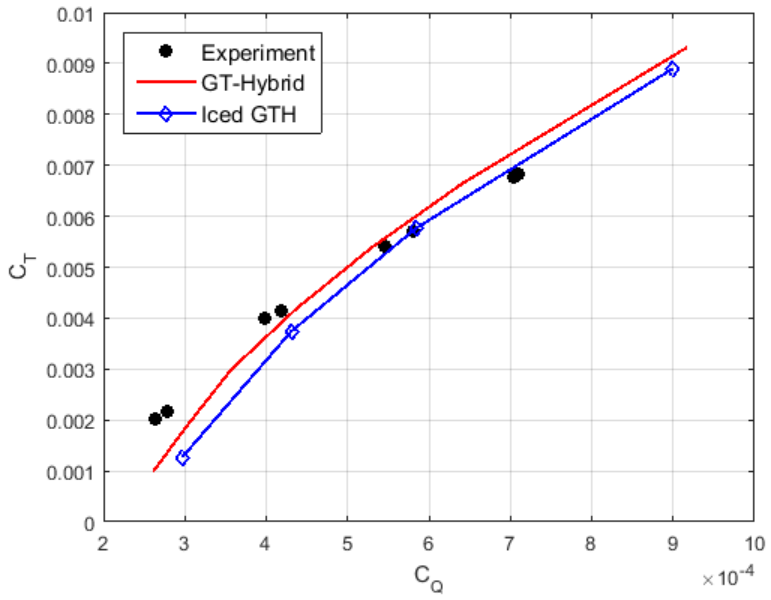

Figure 28 – Thrust coefficient plotted against power coefficient for the coaxial rotor in clean and iced configurations.

Figure 29 shows the figure of merit plotted against the thrust settings. Figure of merit is defined as the ratio of ideal power of a rotor in hover and the actual power consumed. It can be calculated using Equation 8. Although the thrust is shifted toward the right, which means that the thrust increases for each corresponding collective pitch setting, the FM at all thrust setting lies below the clean curve. As it can be seen from the ice shape prediction section, the ice forms at the leading edge of each blade section, increasing the chord length. This may be the reason that for a given collective, the thrust actually increases, but also more than proportionally increased power consumption, leading to a lower figure of merit.

$$FM = \frac{C_T\sqrt{\frac{C_T}{2}}}{C_P} \tag{8}$$

Figure 30 shows the upper and lower rotor figure of merit contributions plotted against the whole rotor thrust for the iced and clean rotor configurations. While the FM for the lower iced rotor decreases relatively a similar amount (5.5% to 7%) at all thrust settings compared to the clean configuration, the upper iced rotor's FM decreases at a lower rate as the thrust setting increases. At lower thrust settings ($C_T \approx 0.0013$) the FM decreases about 19% for the iced rotor, decreases 8% for medium settings ($C_T \approx 0.0037$), and decreases 3% for high settings ($C_T \approx 0.0089$). This difference may be a result of the upper rotor's inflow affecting the lower rotor's performance as it creates a downwash.

Until this study, GT-Hybrid has been used solely for single rotor performance estimation. This study shows that GT-Hybrid can produce acceptable performance and performance degradation predictions for not only single rotors but coaxial rotors as well. It is shown in this section that GT-Hybrid's predictions for the clean rotor matches well with the experimental data especially at lower and medium thrust settings, and also that the performance degradation prediction matches the hypotheses made in Chapter 1.

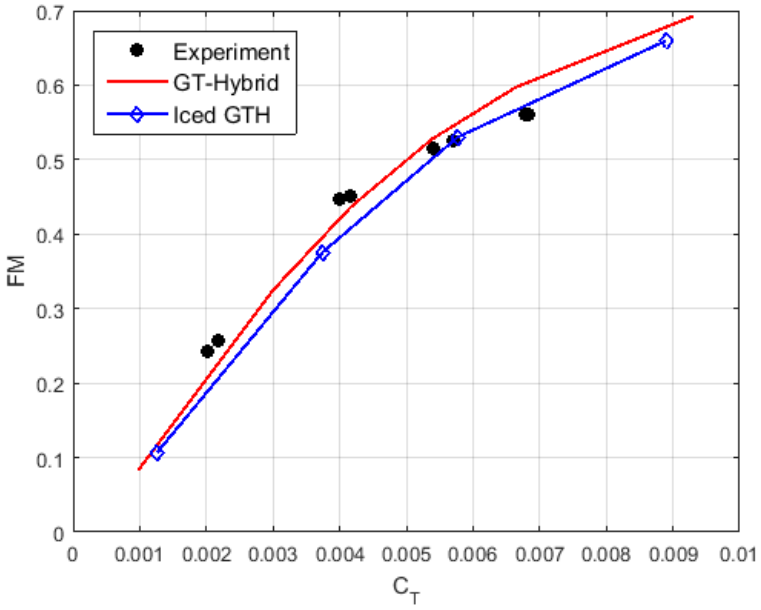

Figure 29 – Figure of merit plotted against thrust for the coaxial rotor in clean and iced configurations.

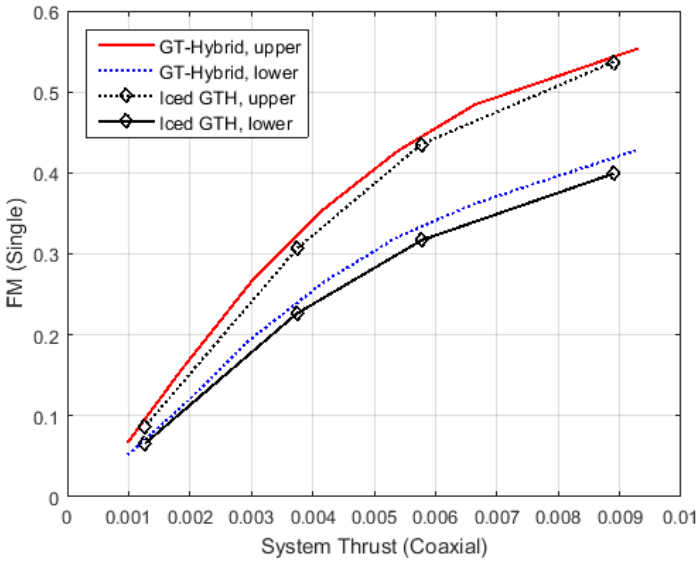

Figure 30 – Figure of merit contributions of upper and lower blade individually versus the total system rotor thrust, including iced rotor results.

CHAPTER 5. CONCLUSIONS AND RECOMMENDATIONS

This study showed ice shape predictions for a single rotor and a coaxial rotor case. The single rotor was modeled from a Bell tail rotor [27] in forward flight, and the coaxial rotor was modeled from Harrington's Rotor 2 [19] in hover. For the Bell tail rotor, the predicted ice shapes were validated by experimental data obtained at NASA Glenn [27]. For the Harrington coaxial rotor, performance results were predicted initially without ice using GT-Hybrid and Star-CCM+, and were compared with experimental values. After simulating the ice shapes on the coaxial rotor, the performance parameters were recalculated using the in-house icing module to predict performance degradation.

The following conclusions may be drawn from this study:

1. For the Bell tail rotor, the numerical and experimental ice shapes agree very well especially at the inboard locations of the blade. As the location advances toward the outboard area, the ice transitions from rime to glaze, forming more complicated structures. Although the current solver is unable to capture all of the details of glaze ice, it can predict the general thickness of ice accurately.
2. For large RPM cases of the Bell tail rotor, the ice is less glaze due to kinetic heating effects. The solver can predict the heating effects well, especially for Run 54. However, additional work is needed for cases with a large RPM and lower static temperatures, as the ice shape is glaze, while the solver predicts a more rime configuration.
3. The performance results for the clean configuration of the coaxial rotor is validated with experimental data. GT-Hybrid results are in good agreement for low to

moderate thrust settings, but slightly underestimate the FM at lower thrust settings and overestimates the FM at higher settings. Star-CCM+ results agree better with the experiment at the higher thrust settings.

4. For the three cases of operating conditions that were tested in the ice accretion of the coaxial rotor, the ice shapes did not vary significantly and were rime ice. More ice was accreted at the tip of the blade compared to the root for all cases.
5. The maximum thickness of the accreted ice is higher at all spanwise locations for the lower rotor than the upper rotor, especially towards the tip ($r/R \approx 0.8$ to 1). This may be an effect of downwash caused by the upper rotor and strong vortices created at the tip.
6. Moderate performance degradation for the iced configuration was observed with GT-Hybrid. For the limited Star-CCM+ cases tested, the obtained results were relatively pessimistic. This opens an opportunity to investigate with other modeling methods and alternate settings for the analyses used.

Based on this study, the following recommendations are made for further research:

1. For the single rotor case, new methods for computing heat transfer rate and skin friction coefficient should be investigated and tested against existing results, in order to produce an icing module that is able to capture glaze ice that are more jagged in physical appearance.
2. More operating conditions should be investigated for ice accretion on the coaxial hover case. This study showed that the current test cases only results in rime ice. Operating conditions that are known to form glaze ice are warm (close to freezing) static temperature, high RPM, and high LWC. The cases tested in this study have a

particularly low RPM and modest collective pitch to match the experimental conditions by Harrington. A variety of combinations of these parameters should be tested to see changes in ice shape and performance.

3. Performance degradation was moderate for the coaxial rotor even with a modest amount of ice, which were also completely rime and not irregularly shaped. Other modeling methods should be pursed to predict performance degradation as well as reconsider some of the settings used in the current and wake-capturing methods. One consideration is to trim the rotor within GT-Hybrid like it is done in the clean configuration simulations. In this study, the rotors were not trimmed due to limitations in computational time.

APPENDIX A. VISCOUS FLOW SIMULATIONS OF COAXIAL ROTORS

Nana Obayashi, Chong Zhou, Lakshmi Sankar and JVR Prasad

School of Aerospace Engineering, Georgia Institute of Technology, Atlanta, GA 30332, USA

Jeewoong Kim

Advanced Rotorcraft Technology, Inc., Sunnyvale, CA 94085, USA

Abstract: Numerical simulations have been conducted for a coaxial rotor tested by Harrington. A wake capturing approach using a commercial Navier-Stokes solver, and a hybrid Navier-Stokes-Free Wake analysis, have been employed. The rotor was trimmed so that the upper and lower rotor torques are equal, cancelling each other. Comparisons with test data and other published data are presented for hover performance over a range of thrust settings. The tip vortex trajectories have also been examined. The hybrid method was computationally efficient and gave acceptable results for hover performance over a range of thrust settings, indicating that this approach is suitable for analysis and preliminary design of rotors. At higher thrust settings, the more costly wake capturing methods were found to be more accurate.

A.1 Introduction

Over the past few years, there has been a growing interest in the use of coaxial rotors for helicopters, with a separate propulsor for propulsion. The use of a coaxial helicopter removes the need for the tail boom and tail rotor. This makes the vehicle compact for a given payload. Retreating blade stall may be eliminated with the use of the advancing

blade concept (ABC). These benefits should, however, by weighed against the structural requirements for the blades, the complex pitch control system, and increased hub drag compared to a single rotor system. An excellent review of the coaxial rotor aerodynamics is presented in Ref. [17].

There is a need to understand and model the aerodynamic, aeroacoustic, and aeroelastic characteristics of these rotor systems. Conventional comprehensive analyses do a very good job of modeling the performance of the coaxial rotors [30, 31, 32, 22, 33], and the interaction of the upper and lower rotor is modeled in these analyses primarily through the trailing wake structures. Vorticity and vortex particle transport equation solvers coupled to a lifting line representation of the coaxial rotor blades have also been employed [34, 35, 36]. Additional work has also been done using physics based models, particularly CFD methods, to better understand the complex physical interaction between the upper and lower rotor [37, 38, 39, 21, 23]. Barbely et al have presented a survey of recent studies related to coaxial rotor phenomena [40].

The present researchers have developed a physics based, computationally efficient, hybrid Navier-Stokes/free wake tool called GT-Hybrid for analyzing conventional and coaxial rotors [41, 42, 43]. This tool complements comprehensive analyses and wake capturing Navier-Stokes analyses developed at NASA, U.S. Army, and by commercial firms. Validation of these tools have been done against wind tunnel and test data for a variety of configurations. Aeroelastic effects of the blades on the hover, forward flight, and maneuvering single rotor configurations are accounted for, by a loose coupling between the present hybrid CFD tools and comprehensive analyses.

The present hybrid methodology is formulated so that single and multi-rotor configurations, including coaxial and tandem rotors, may be readily modeled. Preliminary results for a coaxial rotor in hover, using this methodology, was presented in Ref. [43]. Coaxial rotors in forward flight were studied in Ref. [39]. In the present study, additional applications of this hybrid approach to a coaxial rotor configuration in hover are presented.

A.2 Computational Methodologies

In this section, the Georgia Tech Hybrid Navier-Stokes Methodology is briefly described. Comparisons with a commercial CFD tool called Star-CCM+ has been done as part of this present work. For this reason, this commercial tool is also described.

GT-Hybrid [41, 42, 43] is a finite volume based three-dimensional unsteady viscous compressible flow solver. The flow is modeled by first principles using the Navier-Stokes Methodology. The Navier-Stokes equations are solved in the transformed body-fitted coordinate system using a time-accurate, finite volume scheme. A third-order spatially accurate Roe scheme is used for computing the inviscid fluxes and second order central differencing scheme is used for viscous terms. The Navier-Stokes equations are integrated in time by means of an approximate LU-SGS implicit time marching scheme. The flow is assumed to be turbulent everywhere, and hence no transition model is currently used. The solver accepts a user defined table of blade geometric and elastic deformations and deforms the computational grid. The temporal change in computational cell volume is accounted for, by explicitly satisfying the Geometric Conservation Law (GCL). The near wake region is captured inherently in the Navier-Stokes analysis.

The influence of the other blades and of the trailing vorticity in the far field wake are accounted for, by modeling them as a collection of piece-wise linear bound and trailing vortex elements. The use of such a hybrid Navier-Stokes/vortex modeling method allows for an accurate and economical modeling of viscous features near the blades, and an accurate "non-diffusive" modeling of the trailing wake in the far field.

The vortex model is based on a Lagrangian wake approach where a collection of vortex elements are shed from the rotor blade trailing edge and are convected downstream. The strength of the vortex elements is based on the radial gradient of bound circulation and the number of wake trailers chosen by the user. In case of a single trailer coming off the blade tip, the vortex strength is assumed to be peak bound circulation at the instance the vortex segment is generated. In forward flight, shed wake filaments are also released downstream of the computational domain outflow boundary.

The trailing and shed vortex filaments are propagated in time at a local velocity, calculated as the induced velocity due to all vortex filaments plus the free-stream velocity. The induced velocity due to the free wake structure are also calculated at the N-S computational domain outer surface and are applied as inflow boundary condition at the front, top, and bottom boundaries. This specification of planar velocity field at the inflow boundaries allows the vortices to reenter the computational domain.

Figure 2 shows a schematic view of the Hybrid method employed in GT-Hybrid, depicting the Navier-Stokes domain around the blade-region, the wake captured inside the near-blade Navier-Stokes domain and part of the wake which is modeled as a Lagrangian free wake.

GT-Hybrid currently has the capability to use advanced turbulence models such as SA-DES and KES to compute the eddy viscosity. Although various turbulence models are available in the GT-Hybrid solver, SA-DES model was used in this study for computational efficiency.

This analysis is optionally loosely coupled to complementary computational tools, and works seamlessly with aeroelastic, aeroacoustic, and ice modelling analyses.

Because only the near field is computed using Navier-Stokes equations, the hybrid method is computationally very efficient. Typical CPU time for a given thrust setting varies between 4 and 6 hours for converged solutions on a Linux cluster with 9 nodes (total of 72 cores), with message passing interface (MPI) calls used to exchange data between the individual nodes.

The wake-capturing simulations performed using Star-CCM+ employ a density-based coupled flow solver that is based on the integral form of Navier-Stokes equations. In the present work, spatially second order central differences are used to estimate the inviscid fluxes. A second-order accurate time marching scheme, with dual-time sub-iterations, is employed. The solution was computed for 20 rotor revolutions to convect the starting vortex and initial transients that are an artifact of starting the solution from quiescent flow, out of the flow domain. The air flow has been modeled as a compressible, ideal gas using the classical Reynolds-Averaged Navier-Stokes solver (RANS). The conservation equations for mass and momentum have been solved simultaneously with the coupled flow model, using implicit spatial integration in an unsteady analysis with a coupled algebraic multi-grid method. Menter's k-ω SST model has been used. Further details on the

implementation are available in the documentation for Star-CCM+. The physical time-step must be such that the Nyquist sampling criterion is satisfied, i.e., at least two time-steps per period must be sampled. A physical time step of 1-degree azimuth was used with 15 inner iterations which was found to be sufficient.

A.3 Description of the Coaxial Rotor Configuration

The Harrington coaxial rotors are modeled in present study [19]. Two–bladed, full–scale rotors inside a wind tunnel were tested at Langley full-scale tunnel in 1951. Table 3 gives details of one of these configurations, commonly referred to as Rotor 2 configuration, modeled in this study.

In the experiments, the tests were carried out at two different tip speeds (327 feet/sec and 392 feet/sec). The present calculations were done only for the higher tip speed.

At the cutout (20%R), a NACA 0028 section was used. At the blade tip (100%), the blade section is NACA 0015. It was assumed that the thickness varies linearly between the cutout and the tip. An in-house grid generator was used to generate the body fitted grid for the near field surrounding the rotor blade, as shown in Figure 9.

A.4 Results and Discussions

In this section, selected results for Harrington Rotor 2 are presented. For each thrust setting, the rotor was trimmed within the GT-Hybrid analysis by adjusting the collective pitch of the upper and lower rotor so that the overall thrust coefficient was matched, and the net torque coefficient (sum of the torque on the upper and lower rotors) was zero.

Figure 10 show the computed and measured hover performance of the Harrington 2 rotor. Good agreement between the two analyses is found at low to moderate thrust settings. The GT-Hybrid solver slightly underestimated the figure of merit at lower thrust settings, and consistently overestimated the figure of merit at higher thrust settings. The wake capturing method performs significantly better at the higher thrust settings.

The contribution of thrust, and the corresponding power consumption, from the upper and lower rotors are also of interest. Because the rotor is trimmed for zero net torque, the upper and lower rotors consume equal amounts of power. Thus, the behavior of thrust was first examined. Because the test data only gives the overall rotor thrust, comparisons with test data are not feasible. However, comparisons with Star-CCM+ could be made as shown in the left plot of Figure 11. Very good agreement between the two sets of data is observed.

It is seen that the upper rotor produces considerably more thrust compared to the lower rotor. The linear behavior of this curve suggests that the division of labor between the upper and lower rotors is not affected by the thrust required, at least for the range of thrust settings considered. Since both rotors consume equal amounts of power, the figure of merit of the lower rotor would be expected to be lower than that of the upper rotor. This is indeed the case, as shown on the right plot of Figure 11. CFD results from other researchers, e.g. Ref. [19], have also shown similar behavior.

The inflow modeling may play a critical role in the prediction of power. The sensitivity of the GT-Hybrid predictions to free wake based inflow modeling was examined. The number of trailer elements was parametrically varied, and the number of times that the wake is updated per revolution of the rotor was also examined. Figure 31 and

Figure 32 show the predicted results. Comparisons with other published data20 are also shown. Very small variations in the computed power and figure of merit are seen as these parameters are varied indicating that 10 trailers should be sufficient, with the wake filaments updated every 5 degrees of blade rotation.

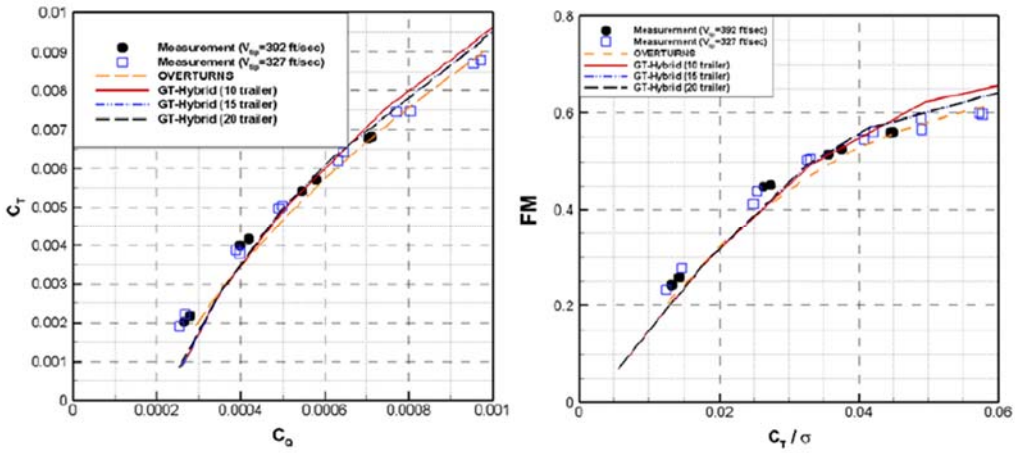

Figure 31 – Effect of number of trailing wake filaments on hover performance.

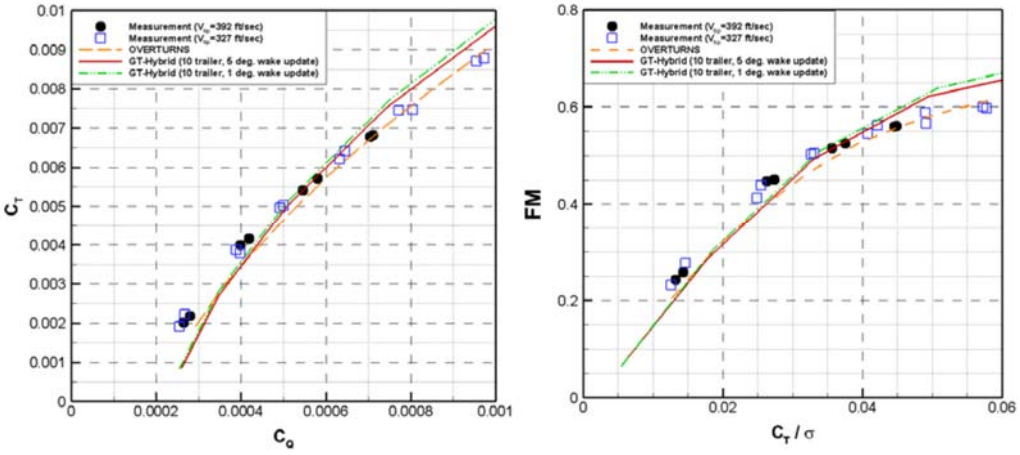

Figure 32 – Effect of wake update on the prediction of hover performance.

Finally, the wake trajectories for the upper and lower rotor, as predicted by GT-Hybrid and Star-CCM+ were examined. Figure 33 shows the vorticity contours from the wake capturing method at a thrust setting of 0.007. The locations of the peak local vorticity were identified and associated with tip vortex structures. As mentioned earlier, GT-Hybrid

uses a free vortex method in the near field with a prescribed far field trajectory model. Star-CCM+ uses a vortex capturing (Eulerian) method. As a result, correlation between the present method and others could only be achieved for the first 200 degrees of vortex age, when the vortex is coherent with a very small vortex core radius. At higher vortex ages, factors such as numerical diffusion and grid density begin to cause deviations.

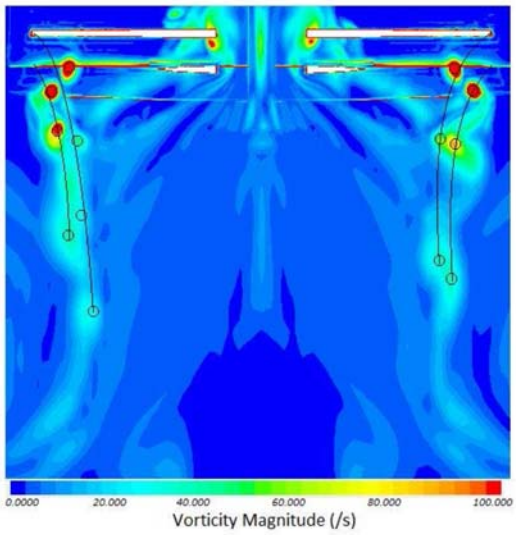

Figure 33 – Tip vortex structures extracted from Star-CCM+ (C_T=0.007).

The hybrid method predicted a somewhat lower descent rate than the vortex capturing method at this thrust setting as seen in Figure 34. This indicates that the GT-Hybrid inflow velocity is lower than that for the wake capturing scheme at this thrust setting (CT=0.007). As expected, the descent rate increases after the first blade passage of 180 degrees, for the upper and lower rotors, both.

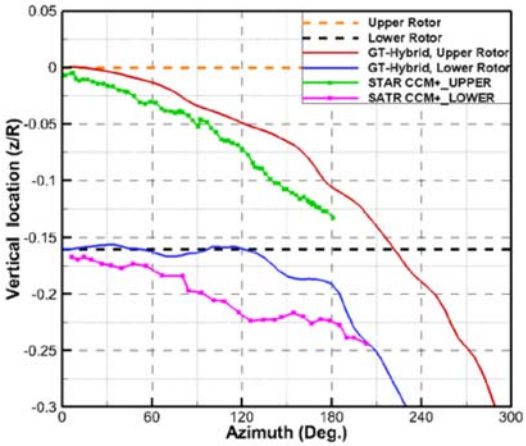

Figure 34 – Tip vortex descent rate as a function of wake age (C_T=0.007).

Figure 35 shows the radial contraction of the tip vortices from the upper and lower rotors at the same thrust setting. Reasonable agreement between the hybrid method and the wake capturing methodology is observed. As expected, the higher thrust generated by the upper rotor leads to a greater contraction rate relative to the lower rotor. The tip vortex from the upper rotor interacts with the lower rotor at the radial position of approximately 85%R at this thrust setting.

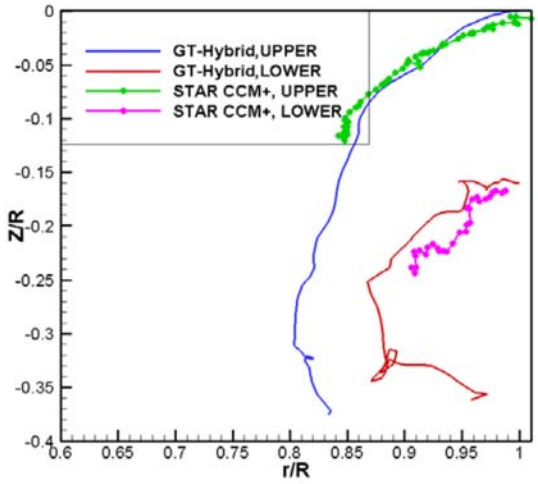

Figure 35 – Tip vortex contraction rate as a function of wake age (C_T=0.007).

A.5 Concluding Remarks

The aerodynamic behavior of a coaxial rotor system has been studied using two approaches – a hybrid Navier-Stokes-free wake solver, and a full wake-capturing approach. Comparisons with test data have been done. The performance of upper and lower rotors, for equal and opposite torque, was examined. Comparisons of the predicted vortex descent rate and radial contraction rate were also examined.

At lower thrust settings, both methods give good agreement with test data. As the thrust level increases, the hybrid method tends to underestimate the power required, and overestimate the figure of merit.

In terms of computational time, the hybrid method is very efficient, requiring 4 to 6 hours of CPU time on a Linux cluster with 72 cores of CPU. The wake capturing method is considerably more expensive. For this reason, the hybrid method is well suited for initial design studies where the rotor geometry is parametrically varied, and quick reasonably accurate solutions are essential. Once a few promising configurations have been identified, more accurate (but computationally expensive) wake capturing simulations may be done to refine the design.

REFERENCES

[1] H. E. Addy, A. P. Broeren, J. G. Zoeckler and S. Lee, "A Wind Tunnel Study of Icing Effects on a Business Jet Airfoil," NASA TM-2003-212124.

[2] H. M. Gurbacki and M. B. Bragg, "Unsteady Aerodynamic Measurements on an Iced Airfoil," in *40th AIAA Aerospace Sciences Meeting and Exhibit*, Reno, NV, 2002.

[3] S. Kumar and E. Loth, "Aerodynamic Simulations of Airfoils with Upper-Surface Ice-Shapes," *Journal of Aircraft,* vol. 38, 2001.

[4] T. L. Miller and T. H. Bond, "Icing Research Tunnel Test of a Model Helicopter Rotor," NASA/TM-101978, 1989.

[5] R. J. Shaw and G. P. Richter, "The UH-1H Helicopter Icing Flight Test Program: An Overview," in *23rd Aerospace Sciences Meeting (AIAA)*, Reno, NV, 1985.

[6] J. G. Leishman, "Coaxial Rotor System," in *Principles of Helicopter Aerodynamics*, New York, NY, Cambridge University Press, 2006, pp. 101-106.

[7] D. P. Guffond, "Icing and Deicing Test on a 1⁄4 Scale Rotor in the ONERA SIMA Wind Tunnel," in *AIAA 24th Aerospace Science Meeting*, Reno, NV, January 1986.

[8] J. D. Lee, R. Harding and R. L. Palko, "Documentation of Ice Shapes on the Main Rotor of a UH-1H Helicopter in Hover," NASA CR 168332, 1984.

[9] W. B. Wright, "User Manual for LEWICE Ver. 3.2," NASA CR 214255, Cleveland, OH, 2008.

[10] R. J. Flemming and D. A. Lednicer, "High Speed Ice Accretion on Rotorcraft Airfoils," NASA CR 3910, 1985.

[11] R. K. Britton, "Development of an Analytical Method to Predict Helicopter Main Rotor Performance in Icing Condition," NASA CR 189110, 1992.

[12] T. Cebeci, "Calculation of Flow Over Iced Airfoils," *AIAA Journal,* vol. 27, pp. 853-861, 1989.

[13] G. Zanazzi, G. Mingione, A. Pagano and A. Visingardi, "Ice Accretion Prediction on Helicopter Rotor Blade in Hover Flight," in *SAE Aircraft and Engine Icing International Conference*, Seville, Spain, 2007.

[14] J. Bain, L. N. Sankar, D. Garza, R. J. Aubert and R. J. Flemming, "A Methodology for the Prediction of Rotor Blade Ice Formation and Shedding," in *SAE 2011 International Conference on Aircraft and Engine Icing and Ground Deicing*, Chicago, IL, June 2011.

[15] R. Narducci and R. E. Kreeger, "Analysis of a Hovering Rotor in Icing Conditions," in *American Helicopter Society 66th Annual Forum*, Phoenix, AZ, May 2010.

[16] R. Narducci, S. Orr and R. E. Kreeger, "Application of a High-Fidelity Icing Analysis Method to a Model-Scale Rotor in Forward Flight," in *American Helicopter Society 67th Annual Forum*, VIrginia Beach, VA, 2011.

[17] C. P. Coleman, "A Survey of Theoretical and Experimental Coaxial Rotor Aerodynamic Research," NASA TP-3675, March 1997.

[18] M. Taylor, "A Balsa-Dust Technique for Air-Flow Visualization and its Application to Flow through Model Helicopter Rotors in Static Thrust," NACA TN-2220, November 1950.

[19] R. D. Harrington, "Full-Scale-Tunnel Investigation of the Static-Thrust Performance of a Coaxial Helicopter Rotor," NACA TN-2318, Washington, 1951.

[20] R. C. Dingledein, "Wind-Tunnel Studies of the Performance of Multirotor Configurations," NACA TN-3236, August 1954.

[21] O. Juhasz, M. Syal, R. Celi, V. Khromov, O. Rand, G. C. Ruzicka and R. C. Strawn, "Comparison of Three Coaxial Aerodynamic Prediction Methods Including

Validation with Model Test Data," *Journal of the American Helicopter Society,* vol. 59, no. 4, pp. 366-381, 2010.

[22] J. Schmaus and I. Chopra, "Aeromechanics for a High Advance Ratio Coaxial Helicopter," in *American Helicopter Society 71st Annual Forum*, Virginia Beach, VA, May 5-7, 2015.

[23] R. Singh and H. Kang, "Computational Investigations of Transient Loads and Blade Deformations on Coaxial Rotor Systems," in *33rd American Institute of Aeronautics and Astronautics Applied Aerodynamics Conference*, Dallas, TX, June 22-26, 2015.

[24] J. Kim, "Development of a Physics Based Methodology for the Prediction of Rotor Blade Ice Formation," SmarTech, Atlanta, GA, 2015.

[25] N. Rajmohan, L. N. Sankar, O. Bauchau, B. Charles, S. M. Makinen and T. A. Egolf, "Application of Hybrid Methodology to Rotors in Steady and Maneuvering Flight," in *AHS International Forum 64*, Montreal, Canada, 2008.

[26] J. M. Hill, in *One-Dimensional Stefan Problems: an Introduction*, Harlow, England, U.K., Longman Science Technical, 1987.

[27] R. E. Kreeger and J.-C. Tsao, "Ice Shapes on a Tail Rotor," in *20th AIAA/CEAS Aeroacoustics Conference*, Atlanta, GA, 2014.

[28] R. Aubert, E. Brouwers, D. Griffiths, P. F. Lorber, R. Narducci, T. Reinert, L. N. Sankar, J. Wright and J. Kim, "High Fidelity Icing Analysis and Validations for Rotors," Charleston, SC, 2015.

[29] N. Obayashi, C. Zhou, S. N. Lakshmi and J. Prasad, "Viscous Flow Simulations of Coaxial Rotors," in *European Rotorcraft Forum*, Lille, France, 2016.

[30] D. A. Wachspress and T. R. Quackenbush, "Impact of Rotor Design on Coaxial Rotor Performance, Wake Geometry and Noise," in *American Helicopter Society 62nd Annual Forum*, Phoenix, AZ, May 9-11, 2006.

[31] J. W. Lim, K. W. McAlister and W. Johnson, "Hover Performance Correlation for Full-Scale and Model-Scale Coaxial Rotors," *Journal of the American Helicopter Society,* vol. 54, 2009.

[32] J. C. Ho, H. Yeo and M. Bhagwat, "Validation of Rotorcraft Comprehensive Analysis Performance Predictions for Coaxial Rotors in Hover," in *American Helicopter Society 71st Annual Forum*, Virginia Beach, VA, May 5-7, 2015.

[33] J. Schmaus and I. Chopra, "Performance and Loads Prediction for High Advance Ration Coaxial Rotor," in *AIAA SciTech Conference*, Kissimmee, FL, January 2015.

[34] H. W. Kim and R. E. Brown, "A Comparison of Coaxial and Conventional Rotor Performance," *Journal of the American Helicopter Society,* 2009.

[35] H. W. Kim, K. Duraisamy and R. E. Brown, "Effect of Rotor Stiffness and Lift Offset on the Aeroacoustics of a Coaxial Rotor in Level Flight," in *American Helicopter Society 65th Annual Forum*, Grapevine, TX, May 27-29, 2009.

[36] J. Zhao and C. He, "Real-Time Simulation of Coaxial Rotor Configurations with Combined Finite State Dynamic Wake and VPM," in *American Helicopter Society 70th Annual Forum*, Montreal, Canada, May 2014.

[37] V. Lakshminarayan and J. Baeder, "High Resolution Computational Investigation of Trimmed Coaxial Rotor Aerodynamics in Hover," in *AHS International Specialists' Conference on Aeromechanics*, San Francisco, CA, January 23-25, 2008.

[38] V. Lakshminarayan, "Computational Investigation of Micro-Scale Coaxial Rotor Aerodynamics in Hover," Ph.D. Dissertation, University of Maryland, College Park, MD, 2009.

[39] T. A. Egolf, N. Rajmohan, E. Reed and L. N. Sankar, "Hybrid CFD Method for Coaxial Rotor Performance in Forward Flight," in *AHS Aeromechanics Specialists Conference*, San Francisco, CA, January 2010.

[40] N. L. Barbely, N. M. Komerath and L. A. Novak, "A Study of Coaxial Rotor Performance and Flow Field Characteristics," in *AHS Technical Meeting on Aeromechanics Design for Vertical Lift*, San Francisco, CA, January 20-22, 2016.

[41] N. Rajmohan, "Application of Hybrid Methodology to Rotors in Steady and Maneuvering Flight," Ph.D. Dissertation, Georgia Institute of Technology, Atlanta, GA, 2010.

[42] R. P. Marpu, L. N. Sankar, S. Makinen, T. A. Egolf, J. D. Baeder and M. Wasikowski, "Physics Based Modeling of Maneuver Loads for Rotor and Hub Design," *Journal of Aircraft,* 2014.

[43] J. Kim, L. N. Sankar and J. Prasad, "Application of a Navier-Stokes Free Wake Hybrid Methodology to the Harrington Coaxial Rotor," in *AHS Technical Meeting on Aeromechanics Design for Vertical Lift*, San Francisco, CA, January 20-22, 2016.

[44] V. K. Lakshminarayan and J. D. Baeder, "High Resolution Computational Investigation of Trimmed Coaxial Rotor Aerodynamics in Hover," *Journal of the American Helicopter Society,* vol. 54, no. 4, October 2009.